



TECHNISCHE
UNIVERSITÄT
WIEN
Vienna|Austria



Diploma Thesis

The mechanical behavior of simple and advanced FDM printed models of human femora

carried out for the purpose of obtaining the degree of Master of Science,
submitted at TU Wien, Faculty of Mechanical and Industrial Engineering, by

Katinka-Marie Biebrich

11742528

Leystasse 81/50, 1200 Wien

under the supervision of

Univ. Prof. Dipl.-Ing. Dr. Dieter Pahr

Institute for Lightweight Design and Structural Biomechanics

Vienna, April 2021

Affidavit

I declare in lieu of oath, that I wrote this thesis and performed the associated research myself, using only literature cited in this volume. If text passages from sources are used literally, they are marked as such.

I confirm that this work is original and has not been submitted elsewhere for any examination, nor is it currently under consideration for a thesis elsewhere.

City and Date

Signature

Acknowledgments

I would like to thank all members of the Department Anatomy and Biomechanics, Division Biomechanics, of the Karl Landsteiner University, in particular my supervisor Prof. Dieter Pahr for his guidance, as well as Lukas Warnung for the constant support.

Appreciation is also extended to the members of the Institute of Lightweight Design and Structural Biomechanics, for many helpful discussions and input, especially Dr. Alexander Synek.

Finally, a special thanks goes to my parents and friends, for their moral support and continuous encouragement throughout my years of study. Without them this achievement would not have been possible. Thank you for always reminding me what is really important in life.

Table of content

<i>Affidavit</i>	ii
Acknowledgments	iii
Table of content	iv
Abstract	vi
Zusammenfassung	vii
List of Figures	ix
List of Tables	xii
List of Abbreviations	xiv
1 Introduction and Motivation	1
1.1 Motivation	1
1.2 Physiology of bones especially the femur	2
1.3 Biomechanics of the human femur	4
1.4 Fracture classifications	6
1.5 Quantitative computer tomography scans	8
1.6 Print Technologies.....	8
1.6.1 <i>Materials used in 3D printing</i>	12
1.6.2 <i>Gyroid pattern</i>	13
1.7 3D printing in biomedical engineering.....	14
1.8 Aim of this work	15
2 Material and Methods	17
2.1 Specimen preparation	19
2.1.1 <i>Image processing of Type 1</i>	20
2.1.2 <i>Image processing of Type 2</i>	20
2.1.3 <i>Image processing of Type 3</i>	21
2.2 3D print and the parameters	25
2.2.1 <i>Used Material</i>	26
2.2.2 <i>Editing of the three types for 3D printing</i>	26
2.2.3 <i>Printing process</i>	33

2.2.4	<i>Post processing</i>	34
2.3	Mechanical testing.....	37
2.4	Data analysis and processing.....	38
3	Results	41
3.1	Influence of reproduction accuracy	41
3.2	Influence of different printing types.....	43
3.3	Influence of different bone sizes	45
3.4	Comparison with real bones	47
4	Discussion	51
4.1	Influence of reproduction accuracy	52
4.2	Influence of different printing types.....	53
4.3	Influence of different bone sizes	53
4.4	Comparison with real bones	54
4.5	Conclusions and Outlook	54
	References	xv
	Appendix A	I
A.1	Test bones.....	I
A.2	Results of the test set of Femur 1 Type 1	II
A.3	Results of the test set of Femur 1 Type 2	III
A.4	Comparison of the results of Femur 1	IV
A.5	Results of the test set of Femur 2 Type 3	V
A.6	Results of the test set of Femur 3 Type 3	VI
A.7	Comparison of the results of Type 3	VII
	Appendix B	VIII
B.1	Supplementary study	VIII

Abstract

Background: Artificial bones are used to perform biomechanical experiments or to validate numerical models. However, currently used artificial bones represent real bones in a very simplified way, which limits their use considerably. The aim of this work was to produce realistic artificial bones by 3D printing, taking into account the cortical thickness and variable bone density within the trabecular region.

Materials and Methods: 3D printed proximal human femora were fabricated using the Fusion Deposition Modeling (FDM) technique with PLA material and a gyroid infill pattern. Maximum force and stiffness were measured with uniaxial compression tests in stance configuration. Existing quantitative CT data (QCT) of three human proximal femora were used as a baseline for image processing. In order to evaluate the influence of accurate reproduction of the real bone, three different complexity types were fabricated, and the mechanical properties were compared, with (1) a constant cortex and a constant infill, (2) a constant cortex with a variable infill, and (3) a variable cortex and a variable infill. In a second step, three femora of one type were compared and in the last step a biomechanical comparison was made with existing results from real bones.

Results: Replicates of human femur could be successfully 3D printed. The more complex the printed type, the higher the accuracy of reproducibility considering the mechanical properties. The different density areas of a bone could be reproduced by a simplified representation of the bone, and lead to a higher maximum force and stiffness. Comparison of the different femora shows that the denser the bone, the higher the maximum force and stiffness. However, when comparing the 3D-printed bones with the three real bones, they behave similarly but as expected much softer. This is because bone tissue has a much higher stiffness and strength compared to PLA. Almost all of the fracture modes of the 3D printed bones showed layer splitting which indicates a relatively poor layer adhesion.

Conclusion: 3D printed bones using FDM technique can reproduce real bones closely in terms of cortical thickness and different density areas. The biomechanical behavior is like real bones, but 3D printed bones are softer. To achieve higher mechanical performance, which is more similar to those of real bones, further adjustments of the printing parameters are necessary. In addition, a different material should be used in the FDM process, as the bone tissue has a much higher stiffness and strength.

Zusammenfassung

Hintergrund: Für die Durchführung biomechanischer Experimente oder zur Validierung numerischer Modelle werden künstliche Knochen verwendet. Derzeit genutzte künstliche Knochen bilden die realen Knochen jedoch sehr vereinfacht ab, was die Verwendung stark einschränkt. Ziel dieser Arbeit war es, realistische künstliche Knochen mittels 3D Druck herzustellen, die die kortikale Dicke und die variablen Dichtebereiche des trabekulären Zentrums berücksichtigen.

Materialien und Methoden: 3D gedruckte proximale menschliche Femora wurden mittels der Fused Deposition Modeling (FDM) Technik aus dem Material PLA mit einer gyroid Füllung hergestellt. Die maximale Kraft und Steifigkeit wurde mit einachsigen Kompressionsversuchen in der Standkonfiguration bestimmt. Vorhandene quantitative CT-Daten (QCT) von drei menschlichen proximalen Femora wurden als Basis für die Bildverarbeitung verwendet. Um den Einfluss von einer akkuraten Abbildung des realen Knochens feststellen zu können, wurden drei unterschiedlich komplexe Typen hergestellt und die mechanischen Eigenschaften miteinander verglichen, wobei (1) eine konstante Kortex und eine konstante Füllung, (2) eine konstante Kortex mit einer variablen Füllung und (3) eine variable Kortex und eine variable Füllung hat. In einem zweiten Schritt wurden drei Femora eines Typs miteinander verglichen und im letzten Schritt wurde ein Vergleich mit vorhandenen Ergebnissen von realen Knochen durchgeführt.

Ergebnisse: Replikat des menschlichen Femurs konnten erfolgreich 3D gedruckt werden. Mit zunehmender Komplexität des gedruckten Typs steigt die Genauigkeit der Reproduzierbarkeit hinsichtlich der mechanischen Eigenschaften. Eine vereinfachte Darstellung des Knochens führt zwar zu einer höheren Maximalkraft und Steifigkeit, stellt aber die einzelnen Dichtebereiche eines Knochens möglicherweise nicht gut dar. Die Gegenüberstellung der verschiedenen Femora zeigt, je dichter der Knochen ist, desto höher ist die Maximalkraft und Steifigkeit. Im Vergleich zu den drei realen Knochen verhalten sich die 3D-gedruckten Knochen jedoch ähnlich, sie sind aber, wie erwartet, weicher. Dies liegt daran, dass Knochengewebe im Vergleich zu PLA eine viel höhere Steifigkeit und Festigkeit aufweist. Fast alle Bruchformen der 3D-gedruckten Knochen zeigten eine Schichtaufspaltungen, dies weist auf eine relativ schlechte Schichthaftung hin.

Schlussfolgerung: Mit der FDM-Technik gedruckte 3D-Knochen können echte Knochen in Bezug auf die kortikale Dicke und die verschiedenen Dichtebereiche realitätsnah reproduzieren. Auch das biomechanische Verhalten ist ähnlich dem echter Knochen, allerdings sind 3D-gedruckte Knochen weicher. Um eine höhere mechanische Performance zu erreichen, die den echten Knochen mehr entspricht, sind weitere Anpassungen der Druckparameter notwendig. Außerdem sollte ein anderes Material für den FDM Prozess verwendet werden, da das Knochengewebe eine wesentlich höhere Steifigkeit und Festigkeit aufweist.

List of Figures

Figure 1: Human femur at its proximal end with an anterior, posterior, and medial view from left to right [6].	2
Figure 2: Left: Proximal human femur with trabecular (inside) and cortical bone (outside). [8] Spongy bone on the right side [4]. Right: View of the spongy and compact bone structure. Adapted from [4].	3
Figure 3: Hierarchical structure of the cancellous bone [11].	3
Figure 4: Mechanical test setup of a single-leg stance (left) and a fall configuration (right) [21].	5
Figure 5: Anatomical (left) and mechanical (right) axis of the femur. Adapted from [22].	6
Figure 6: Left: Division of the human femur into three sections. Right: Division of the proximal end segment into three sections. Both adapted from [26].	6
Figure 7: Overview of all fractures of the proximal end segment of the human femur classified by the AO foundation [27].	7
Figure 8: Steps of generating a 3D model.	9
Figure 9: FDM principle [40].	11
Figure 10: Selectable infill patterns in <i>Prusa Slicer</i> [45].	13
Figure 11: 3D printed <i>gyroid</i> structure with zoom in on the right side.	13
Figure 12: Study design.	16
Figure 13: Femur with a displacement of 20° to the anatomical axis. On the left side the force angles during a gait cycle, measured by the OrthoLoad lab (Charitè, Berlin, Germany). On the right side the representation of the 20° difference to the anatomical axis.	18
Figure 14: The three different types of one femur. From left to right: Type 1, Type 2, Type 3 with zoom into the various infill densities.	18
Figure 15: Overview of the process framework of the three types. The pictures show <i>Femur 1</i> .	20
Figure 16: Interpolated computed values based on a background grid [56].	22
Figure 17: All three femora with the different separated grey values for different densities.	23
Figure 18: Mapped density areas of the three femora with the resulting histograms.	24

Figure 19: Cross section of the trabecular centers of the three different femora, on top the real density distribution, on the bottom the three resulting density area maps. From left to right: <i>Femur 1, Femur 2, Femur 3</i>	25
Figure 20: Technical drawing of the spacer with a hole for the alignment.....	26
Figure 21: <i>Femur 1 Type 1</i> with 16% gyroid infill and constant cortex	29
Figure 22: Left: Infill (left) and cortex (right) of <i>Femur 1 Type 2</i> ; Right: <i>Femur 1 Type 2</i> with 16% gyroid infill and variable cortex.....	30
Figure 23: Three infill regions and the cortex of <i>Femur 1 Type 3</i>	31
Figure 24: Left: <i>Femur 2 Type 3</i> with three differently mapped density areas and a variable cortex. Right: <i>Femur 3 Type 3</i> with three differently mapped density areas and a variable cortex.	32
Figure 25: <i>Femur 1 Type 1 & 2</i> during the printing process and right the infill of <i>Femur 3 Type 3</i>	33
Figure 26: Left: Used vice needed to remove an edge of the bones. Middle and right: Removed edge of the shaft.	34
Figure 27: Left: Aligned and embedded femur. Right: Femur in drill stand with embedding of the head.	35
Figure 28: Tool for embedding of the shaft on the left and turned fixture and the cups for the embedding of the head on the right.....	35
Figure 29: Embedded femur at the top and bottom.....	36
Figure 30: Measuring points of the bone for example on <i>Femur 1 Type 1</i>	36
Figure 31: Experimental setup for STANCE configuration of the femur.....	38
Figure 32: Schematic load- displacement curve for a bone, where F is load and d is displacement. The stiffness is calculated from the linear region.	39
Figure 33: Results of the test set of <i>Type 3</i> of <i>Femur 1</i>	42
Figure 34: <i>Type 3</i> of <i>Femur 1</i> of all test runs, from left to right: test 1, test 2, test 3.	43
Figure 35: Results of <i>Femur 1</i> for the selected three different 3D printing types.	44
Figure 36: From left to right Type 1, Type 2, Type 3 of <i>Femur 1</i>	45
Figure 37: Results of Type 3 for all three femora.	46
Figure 38: From left to right <i>Femur 1, Femur 2, Femur 3</i> of all femora.....	47
Figure 39: Results of Type 3 for all three femora and results of all three real femora.	48
Figure 40: Mean value of the max. force of the 3D printed bones and max. force of the real bones.....	49

Figure 41: Mean value of the stiffness of the 3D printed bones and stiffness of the real bones.	50
Figure 42: Splitting of the test bone with a non-embedded head.....	52
Figure 43: Left: Results of the test bones. Middle: Fracture of the vertical printed test bone. Right: Splitting of the head of the first horizontal printed testbone.....	I
Figure 44: Left: Results of <i>Type 1</i> of <i>Femur 1</i> . Right: <i>Type 1</i> of <i>Femur 1</i> of all test runs, from left to right: test 1, test 2, test 3	II
Figure 45: Left: Results of <i>Type 2</i> of <i>Femur 1</i> . Right: <i>Type 2</i> of <i>Femur 1</i> of all test runs, from left to right: test 1, test 2, test 3	III
Figure 46: Mean values of all types of <i>Femur 1</i>	IV
Figure 47: Left: Results of <i>Femur 2 Type 3</i> . Right: <i>Type 3</i> of <i>Femur 2</i> of all test runs, from left to right: test 1, test 2, test 3	V
Figure 48: Left: Results of <i>Femur 3 Type 3</i> . Right: <i>Type 3</i> of <i>Femur 3</i> of all test runs, from left to right: test 1, test 2, test 3	VI
Figure 49: Left: Mean values of <i>Type 3</i> of all three femora. Right: <i>Type 3</i> of all femora. From left to right: <i>Femur 1</i> , <i>Femur 2</i> , <i>Femur 3</i>	VII
Figure 50: Top: Results of the comparable bones. Bottom: From left to right: SLA printed bone, <i>ORTHObone</i> and <i>PET</i> printed bone.....	X

List of Tables

Table 1: Mechanical properties of bone under compression [15]	4
Table 2: Mechanical properties of cortical bone. Adapted from [16].	4
Table 3: 3D printing classifications with technology and material examples according to ASTM standard [36, 39]	10
Table 4: Properties of PLA, PETG and ASA according to <i>Prusa</i> [41, 42, 44]	12
Table 5: Summary of the experimental data of the three femora [20].	17
Table 6: Summary of the properties of the printed bone types. Each type is printed three times per femur.	19
Table 7: Sum of grey values and mean density of the trabecular center	21
Table 8: Mapped density areas in relation to the number of bins.	23
Table 9: Properties of PLA vanilla white according to the technical sheet [44].	26
Table 10: Indicated values of the volume and the surface from the <i>3D Tool</i> for <i>Femur 1</i> and the infill of <i>Femur 2</i>	28
Table 11: Calculated parameters for the settings	29
Table 12: Settings of the three types of <i>Femur 1</i>	31
Table 13: Settings of <i>Type 3</i> of all femora	32
Table 14: Summary of the print time and used filament of all femora.	33
Table 15: Comparison of calculated weight from <i>Prusa Slicer</i> and mean value of measured weight with standard deviation.	34
Table 16: Details of the three types of <i>Femur 1</i> for all three test series, as well as for <i>Type 3</i> of <i>Femur 2</i> and <i>3</i>	37
Table 17: Maximum force and stiffness of the test set of <i>Type 3</i> of <i>Femur 1</i>	42
Table 18: Maximum force and stiffness of all types of <i>Femur 1</i> with the mean value with standard deviation.	44
Table 19: Maximum force and stiffness of all <i>Type 3</i> of all femora with the mean value with standard deviation.	46
Table 20: Results of the experiments of the three real femora.....	50
Table 21: Results of maximum force and stiffness of the test bones.	II
Table 22: Maximum force and stiffness of the test set of <i>Type 1</i> of <i>Femur 1</i>	II
Table 23: Maximum force and stiffness of the test set of <i>Type 2</i> of <i>Femur 1</i>	III

Table 24: Average and coefficient of variation of maximum force and stiffness for all three types of <i>Femur 1</i>	IV
Table 25: Maximum force and stiffness of the test set of <i>Type 3</i> of <i>Femur 2</i>	V
Table 26: Maximum force and stiffness of the test set of <i>Type 3</i> of <i>Femur 3</i>	VI
Table 27: Average and coefficient of variation of the maximum force and stiffness for <i>Type 3</i> of all femora	VII
Table 28: Properties of PET according to the manufacturer [61].	VIII
Table 29: Details of the bone printed with PET and SLA printed bone and the <i>ORTHObone</i>	IX
Table 30: Max. force and stiffness of the comparable bones and the average of <i>Femur 1 Type 2</i> and <i>Femur 2 Type 3</i>	X

List of Abbreviations

ASA	Acrylonitrile Styrene Acrylate
CAD	Computer Aided Design
CT	Computer Tomography
FDM	Fused Deposition Modelling
MRI	Magnetic Resonance Tomography
PCL/HA	Polycaprolactone/ Hydroxyapatite
PEEK	Polyether Ether Ketone
PET	Polyethylene Terephthalate
PLA	Poly lactide
QCT	Quantitative Computer Tomography
SLA	Stereolithography
STL	Stereolithography Interface Format
w/	with
w/o	without

1 Introduction and Motivation

1.1 Motivation

For many years, biomechanics has been concerned with the mechanical behavior of bones. For such studies, real bones, artificial bones, or simulation models are used.

Artificial bones are used for biomechanical studies and to validate simulation models. A major advantage is the repeatability of experiments. The use of artificial bones offers the possibility to investigate biomechanical properties of patient-specific models or to multiply selected models as many times as desired. Patient-specific models can be produced in the own laboratory using a simple and cost-effective manufacturing process (e.g., FDM). A drawback is that the artificial bones often have only a very simplified internal structure. Thereby it is disregarded that the trabecular center has a varying density and a varying degree of anisotropy. In most cases, the artificial bone is only provided as an isotropic sponge with a uniform density. Thus, the models are sufficient to detect the haptics and components but are less suitable for mechanical testing and will be used mostly for teaching [1]. However, due to this simplified illustration of the material properties, it is possible that the results of the tests done with the artificial bones are inaccurate or not feasible.

3D printing has become an increasingly popular technology in the last years and can be found in many areas of industry and science [2]. This type of manufacturing is also conceivable for making an artificial bone from clinical CT images. Depending on the printing process, a realistic bone with a varying thickness of the cortex and different density areas in the trabecular center can be represented and then mechanically tested. The goal of this thesis was to accurately represent real bones, in terms of infill density and cortical thickness by using the fused deposition modelling technique, to experimentally test the biomechanical performance and then compare them with those of the real bones.

1.2 Physiology of bones especially the femur

Bones are the framework of our body, there are different classifications of bones that together represent the skeleton. The classification is based on the shape, so there are four different classes, the long bone, short bone, flat bone and irregular bone. Additionally, there are several functions of bones, among other things, they are responsible not only to form the skeleton, but to protect soft parts of the body. They are also able to withstand forces or to transmit them. And together with the muscles, a movement is generated [3, 4].

The pelvic girdle and the free lower limbs, consisting of femur, crus and pes, form together the skeleton of the lower extremity. The femur is located with the head in the pelvic girdle [5] and belongs to the class of long bones. In Detail, as shown in Figure 1, the human femur is subdivided into head, neck, greater and lesser trochanter, and the typical fovea capitis femoris [6].

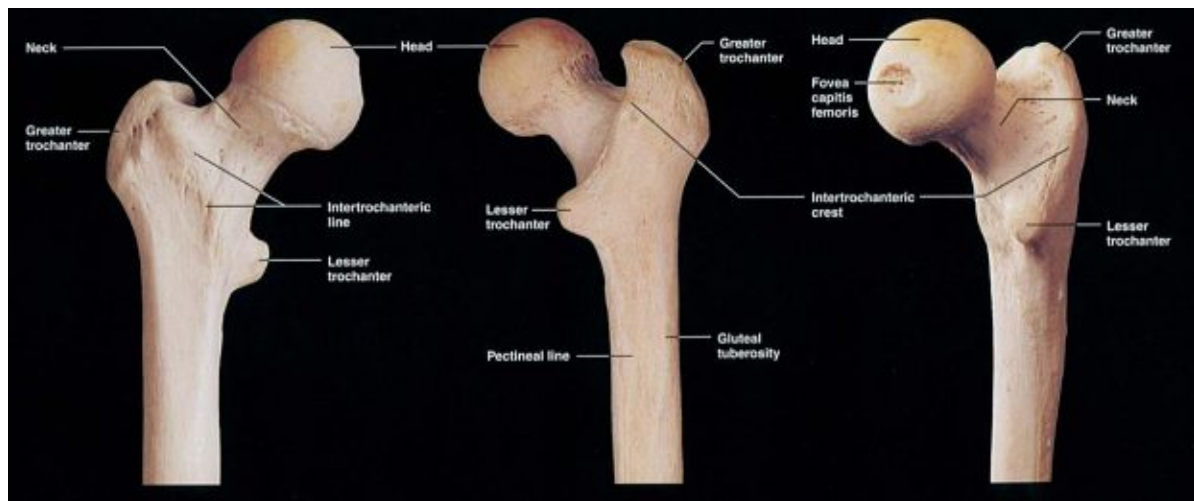


Figure 1: Human femur at its proximal end with an anterior, posterior, and medial view from left to right [6].

Considering bones at the macro level, they have an outer layer, the cortex or compact bone, which surrounds the infill of the bone, the cancellous bone, commonly known as spongy bone, both illustrated in Figure 2. The cortical bone is mainly found in the shaft of the long bones, whereas the trabecular bone is mainly found at the end of the femur [7].

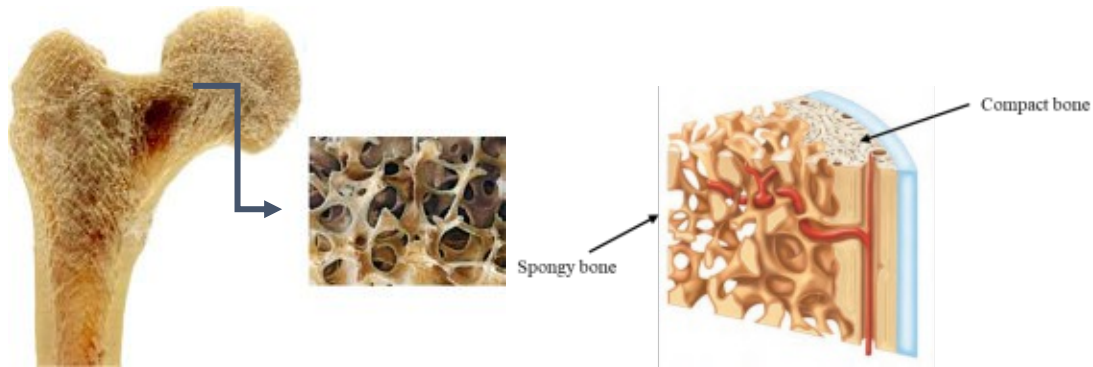


Figure 2: Left: Proximal human femur with trabecular (inside) and cortical bone (outside). [8] Spongy bone on the right side [4]. Right: View of the spongy and compact bone structure. Adapted from [4].

Cancellous bone, the inner part of the femur, has a differentially packed structure, which in the living organism is filled with red or yellow bone marrow [4, 9]. The inner structure has an anisotropic material behavior, is less dense and less stable than the outer cortex, which has only microscopically small channels but has also a variable thickness [7], as seen on the right side of Figure 2. The function of the cortex is mainly to protect the inner part of the bone. The cancellous bone shows a kind of lattice structure of several small plates and rods, the so-called trabeculae, which consist of collagen fibrils, as seen in Figure 3. Even though the arrangement of the trabeculae seems random, they adapt very well to the stress pattern and can thus withstand great loading [3, 4]. This causes the structure of the cancellous bone to be very complex, in addition to the fact that the arrangement of the structure can also change due to age, gender or even anatomical location [10].

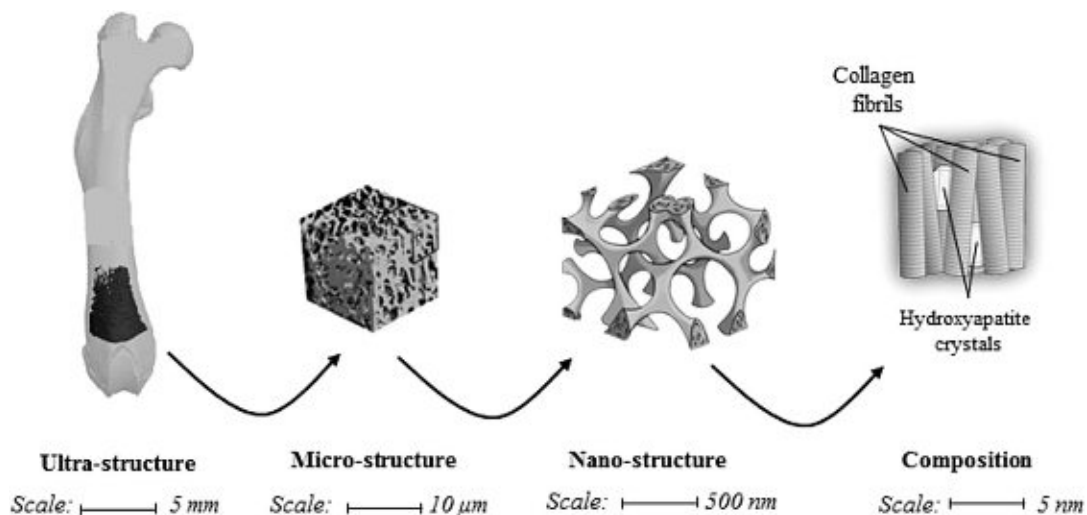


Figure 3: Hierarchical structure of the cancellous bone [11].

Although it is made of less material, the inner part of the bone has the ability to withstand loads and therefore serves as a model for the construction of the Eiffel Tower [12].

1.3 Biomechanics of the human femur

Due to the different composition and microstructure, which show a variation in several anatomical locations, bone is an anisotropic and inhomogeneous material [13]. The mechanical properties of a bone thus depend on the material and the density of this material, as well on the applied load. Bones can actively adapt to the applied load and thus change their mechanical properties. To understand these material properties in vivo, it is necessary to perform in vitro tests [14]. T. Kokubo et al. presented the mechanical properties of cancellous and cortical bone in their paper, which are shown in Table 1 [15].

Table 1: Mechanical properties of bone under compression [15]

Human bone	Compressive strength in MPa	Young's modulus in GPa
Cancellous	2-12	0.05-0.5
Cortical	100-230	7-30

The mechanical properties, such as stiffness and strength, of cortical bone depend on the direction of the applied load. Thus, the bone achieves a higher stiffness longitudinally to the bone axis than transversely, as seen in Table 2. In addition, Reilly et al. [16] found in their study that cortical bone is stronger in compression than in tension.

Table 2: Mechanical properties of cortical bone. Adapted from [16].

Parameter	Value
Modulus in GPa	
Longitudinal	17
Transversal	11.5
Ultimate strength: longitudinal in MPa	
Tension	133
Compression	193
Ultimate strength: transverse in MPa	
Tension	51
Compression	133

The mechanical properties of trabecular bone strongly depend on the volume fraction, trabecular tissue material properties and its structure [11]. The characteristics additionally are dependent on age, gender or diseases [17].

The values listed are given as an indication of the magnitude. Since the measured mechanical properties depend strongly on the measuring method and the way the test is performed.

There are many different methods of biomechanically testing a femur. It is possible to test the entire femur [18] or only the proximal region, by putting the femoral neck under stress. Cortical and trabecular structures in the femoral neck vary depending on the load condition [19]. Several studies investigate the mechanical properties when comparing the two load configurations [19–21]. The bone can be loaded both in the standing (STANCE) position and in the lying (SIDE) position, both shown in Figure 4. For both types, the shaft is fixed, for example by a fixed clamping in the tensile testing machine with an additional embedding. A compression test simulates the different loads on the femur [20].

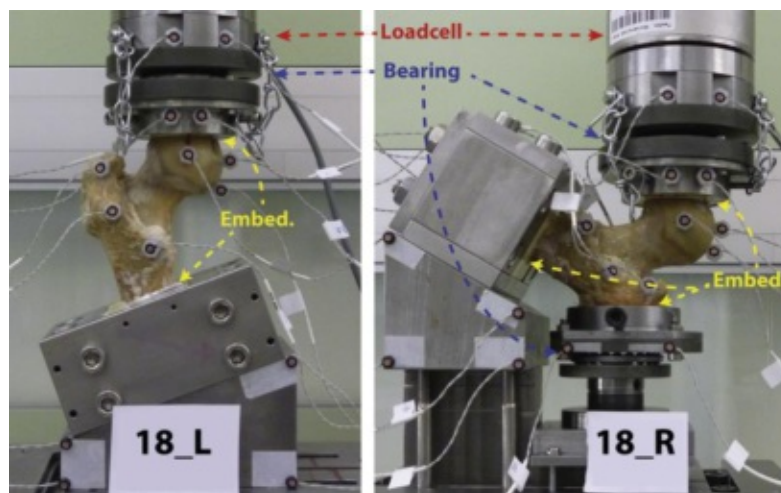


Figure 4: Mechanical test setup of a single-leg stance (left) and a fall configuration (right) [21].

In the study by Dall'Ara et al. the bones were measured in the STANCE position to simulate a one-legged stance configuration. In the STANCE position, the force does not apply directly on the anatomical axis of the femoral head, instead it is applied with an angle. For this purpose, the bones were biomechanically tested with an angle of 20° to the anatomical axis [20]. The femur has two axes. The mechanical axis extends from the center of the femoral head to the center of the knee joint, as shown in Figure 5 on the right. The mechanical axis has a 6° deviation from the anatomical axis, which passes through the center of the femur and is also called the midshaft line [5].

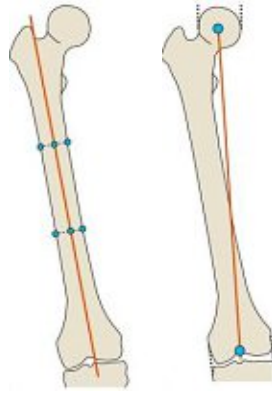


Figure 5: Anatomical (left) and mechanical (right) axis of the femur. Adapted from [22].

Testing the STANCE configuration is important to see how the bone behaves during daily movements and under which forces spontaneous fractures occur, without any trauma [23]. Applying the load to the femoral head causes an artificial fracture and the material to displace. As a result, a load- displacement curve is recorded with several other parameters.

1.4 Fracture classifications

Bone disease can have a major impact on the quality of life [15]. Osteoporosis is a very common disease, which involves the risk of bone fractures [24]. This can be due to the bone density, which decreases with age. The risk of fracture increases with lower bone density. These properties of the bone can be identified, for instance, using the bone imaging method QCT, which is described in detail in chapter 1.5 [25].

The AO foundation provides an overview of the fracture types of long bones. The human femur is divided into three parts, as shown in Figure 6. First is the distal end segment, where the femur and patella meet, next is the diaphyseal segment, which is the shaft of the femur, and lastly the proximal end segment, where the femoral head is located [26]. Following is a more detailed explanation of the individual fractures of the proximal end segment.

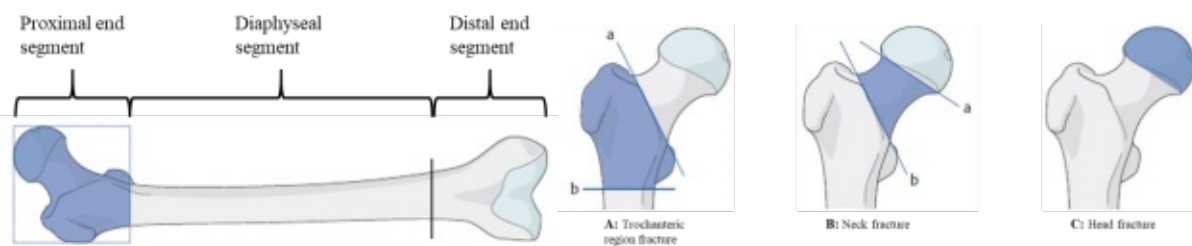


Figure 6: Left: Division of the human femur into three sections. Right: Division of the proximal end segment into three sections. Both adapted from [26].

The proximal end segment is split into three parts. In Figure 6, these parts are labeled A, B, C and represent the different fracture regions. Type A is the trochanteric region fracture, type B the neck fracture and type C the head fracture. The highlighted areas are the regions in which the fracture occurs.

These three types are further split up into individual subgroups, where the actual fractures are shown with their labels. Type A and B have again three subgroups, type C has two subgroups, all shown in Figure 7. Based on this classification, the fractures of the proximal end segment of the human femur can be clearly identified and categorized.

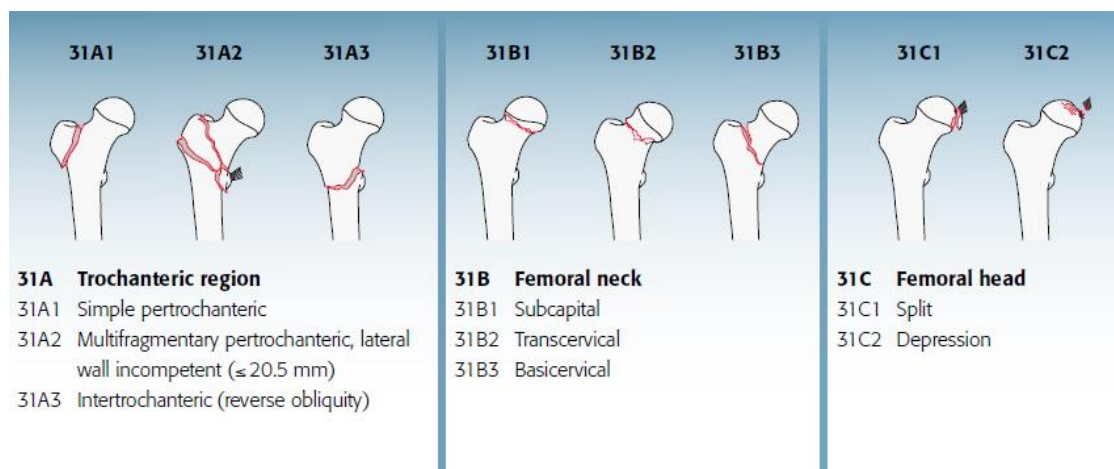


Figure 7: Overview of all fractures of the proximal end segment of the human femur classified by the AO foundation [27].

The three subgroups of type A, trochanteric region fracture, differ greatly in the location of the fracture. In the simple petrochanteric fracture group, the fracture line begins on the greater trochanter and extends to just above or just below the lesser trochanter. Special here is that the bone splits in two parts and the fracture remains very stable after fixation. In the second subgroup, multifragmentary petrochanteric, the fracture also starts at the greater trochanter and extends to the medial cortex, here the bone is split into three parts. In the third subgroup, intertrochanteric fracture, it should be highlighted that the fracture runs between the two trochanters [26].

Type B, the neck fracture, is also divided into three subgroups. In the first subgroup, the subcapital fracture, there is no or only a small displacement and the contact between head and neck is always present. A special case is the displaced fracture, which is intracapsular and usually stops the blood supply. In the subgroups transcervical and basicervical fracture, the rupture begins slightly below the head, which can result from adduction injuries [26].

Type C, the head fracture, is divided into two subgroups. The first is the split fracture, which is usually associated with hip joint dislocation and disrupts the blood supply. The second subgroup, depression fracture, is often related to an anterior hip dislocation, usually requiring surgical procedure [26].

1.5 Quantitative computer tomography scans

Computed tomography (CT) is a 3D imaging technique and can be used to generate in vivo images of mainly hard tissue. This technique is based on the X-ray absorption of tissue, which is measured in Hounsfield Units (HU). The reference value is water with a value of 0 HU. Bones consist of materials with a high atomic number, the so called voxels, these materials absorb more X-rays and are shown as a white region in the CT image [28].

Quantitative computer tomography (QCT) is a technique to measure bone mineral density (BMD) in 3D, this indicates the mechanical competence of the bone. Compared to plane dual-energy X-ray absorptiometry (DXA), which is widely used, QCT scans can separately detect cortical and trabecular BMD [28]. The resulting QCT images have a voxel size in the sub-millimeter range [29].

The greyscale images obtained from the QCT can be read, converted, and further processed using image processing. In the simplest case, one can segment such image data and export the outer bone surface as STL to 3D print the shape [30]. More detailed approaches allow a differentiation between cortical and trabecular bone, which is why both parts of the bone can be segmented separately. Furthermore, the infill density could be linked to the bone density [30, 31].

1.6 Print Technologies

3D printing is a cost-effective technique for producing three-dimensional objects, which often have a complex geometry [2]. In many industrial sectors this comparatively fast process is used for prototype production and to detect possible errors [32].

3D printing can currently be found in many areas of the healthcare sector [33]. This process can be used not only to produce surgical instruments or implants, but to visualize complex structures. 3D printed models are also used in medicine in order to better plan complicated surgeries and to effectively train staff in this area [33].

CT or MRI data can be converted into STL files to create a 3D printed model. Using this technique, it is also possible to register the aesthetics of the surgery and the difficulties during the operation in advance. Implants printed in 3D must be sterilizable and biocompatible to be used in vivo [2]. The four major fields of applications of 3D printing in medicine are surgical instruments, models for surgery, individual prostheses, and the production of tissues and organs. However, the last of these is done in 3D bio-printers especially designed for this purpose. In this process usually no plastic or metal is printed, but living cells are used in combination with scaffolds [34].

The geometry of these objects is done by creating a CAD model or using segmented CT data, as described in the previous chapter, resulting in a STL file [35]. By using a slicing software (e.g., *Prusa Slicer*, Prusa Research, Prague, Czech Republic), the previously constructed model is then divided into individual layers with definable thickness and infill pattern. The setting of various print and printer parameters can also be adjusted. The resulting 3D print file, which contains all information for the printer, is then exported and printed. Component quality and accuracy depend on various parameters, including the CAD design itself, the material, the printer, and the experience of the operator. The variety of setting options, maintenance before printing and the post-processing of the print itself have a huge influence on the quality [2]. The steps just listed are summarized in Figure 8.



Figure 8: Steps of generating a 3D model.

ASTM Standard F2792-12a divides 3D printing into seven categories, binder jetting, direct energy deposition, material extrusion, material jetting, powder bed fusion, sheet lamination and vat photopolymerization [36].

All following definitions are based on the ASTM standard F2792-12a and can be seen in Table 3 [36]. In binder jetting, powder particles are bonded at selected points with a liquid binder to form parts or objects. This lists the category of additive manufacturing, as well as corresponding examples and materials.

Direct energy deposition is a more complex process. In this process, thermal energy is used to unite materials by melting them together during deposition.

In material jetting, droplets of the material are selectively applied under ultraviolet light [37]. In powder bed melting, thermal energy selectively melts areas of a powder bed. This can be realized either with an electron beam or a laser [37].

In sheet lamination, separate layers of material are bonded together to form an object, allowing complex geometries to be represented.

In vat photopolymerization, liquid photopolymer is selectively cured in a vat by light-activated polymerization. A well-known example of this is stereolithography (SLA). The SLA technique has a high accuracy and can be used with different materials. A laser beam is used to illuminate the resin with a pattern and a previously defined depth and then is hardened. New resin is added afterwards, and the procedure is repeated layer by layer. The field of application ranges from automotive and jewelry to the biomedical field including the manufacturing of implants [38].

Table 3: 3D printing classifications with technology and material examples according to ASTM standard [36, 39]

Category	Technology examples	Used Material examples
Binder jetting	3D printing, ink- jetting	Metal, polymer, ceramic
Direct energy deposition	Laser deposition, electron beam direct melting	Metal: powder and wire
Material extrusion	Fused deposition modelling (FDM)	Polymer
Material jetting	Polyjet, ink- jetting	Photopolymer, wax
Powder bed fusion	Selective laser sintering (SLS), selective laser melting (SLM), electron beam melting (EBM)	Metal, polymer, ceramic
Sheet lamination	Laminated object manufacturing, ultrasonic consolidation	Metal, ceramic
Vat photopolymerization	Stereolithography (SLA), digital light processing	Photopolymer, ceramic

Fused deposition modeling (FDM) is commonly known as fused layer modeling (FLM), it is one of the older methods and a very popular 3D printing technique that belongs to the category material extrusion. In this procedure, the solid coiled plastic is melted in an extruder, which is a heated nozzle, and then applied layer by layer, as seen in Figure 9 [2]. Due to the heat conduction the plastic hardens in the applied form, which the nozzle moves in x- y- direction and hardens afterwards. The three-dimensional form is created by layering the individual layers one upon the other [32]. For suspended parts or overhangs there is also the possibility of printing supports, which can be broken away after cooling [2]. The material is pulled in by rotating wheels with a constant velocity and then melted in the extrusion head before being applied to the print bed, or the previous layer, by the nozzle. With this technique, it is possible that the support material is different from the build material. This depends on the individual printer and the print to be performed.

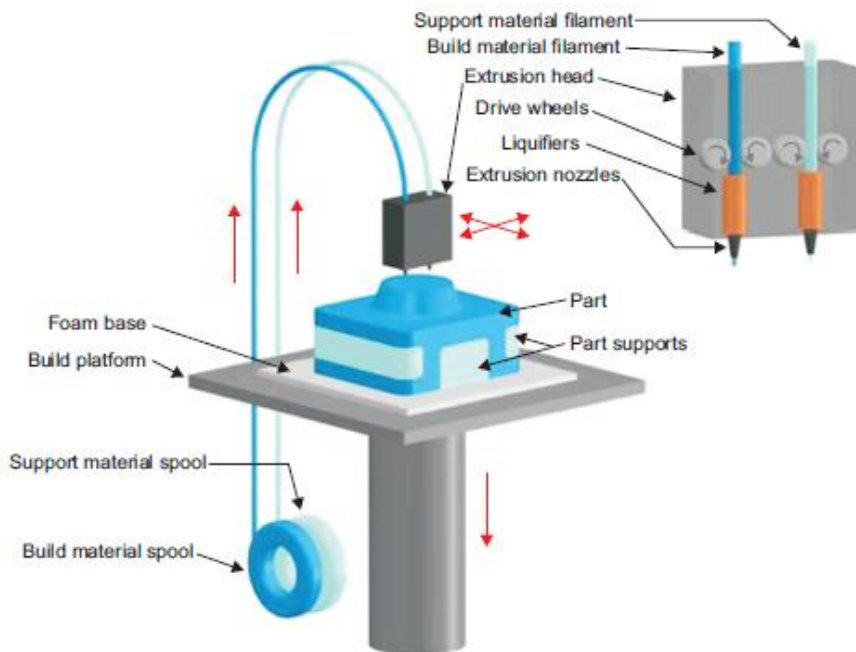


Figure 9: FDM principle [40]

By using 3D printing it is possible to adjust many parameters, which can influence the strength and ultimate force. The material also has a significant role, as well as the chosen pattern.

1.6.1 Materials used in 3D printing

The choice of material is essential for 3D printing using FDM, as it has a direct impact on the mechanical properties of the model. The most commonly used materials are thermoplastics such as PETG, PLA or ASA.

PETG (polyethylene terephthalate) is a copolymer of PET mixed with glycol and is one of the most widely used polymers. It is a more heat resistant, flexible, less brittle but also a more expensive material compared to PLA [41].

ASA (acrylonitrile styrene acrylate) is heat resistant and well suited for high mechanical stress. However, it is more complicated to print for larger parts [42].

PLA (Polylactic acid) is the most commonly used filament for 3D printing. It is characterized by a low melting temperature and is derived from renewable resources, so it is biodegradable as well [43]. PLA is also stiff, cheap and easy to print, and additionally robust against impact [44].

When comparing the specifications of *Prusa's* (Prusa Research, Prague, Czech Republic) filaments, it can be seen that on a price per kilo, PLA is the cheapest material and has the highest strength, tested according to ISO 527. Table 4 shows some properties of the three filaments from *Prusa* [41, 42, 44].

Table 4: Properties of PLA, PETG and ASA according to Prusa [41, 42, 44]

	PLA	PETG	ASA
Density in g/cm ³	1.24	1.27	1.07
Price/kg in €	25	30	35
Tensile yield strength filament in MPa (ISO 527-1)	57.4 ± 0.4	46 ± 1	40 ± 1

1.6.2 Gyroid pattern

Time and material can be saved by a low percentage of infill, but this has to be chosen in relation to good mechanical properties. The infill pattern also has a major role in this [45]. In the slicing software *Prusa Slicer*, 13 different infill structures can be selected for the FDM printing method, as shown in Figure 10. The infill density can be set between 0 and 100%.

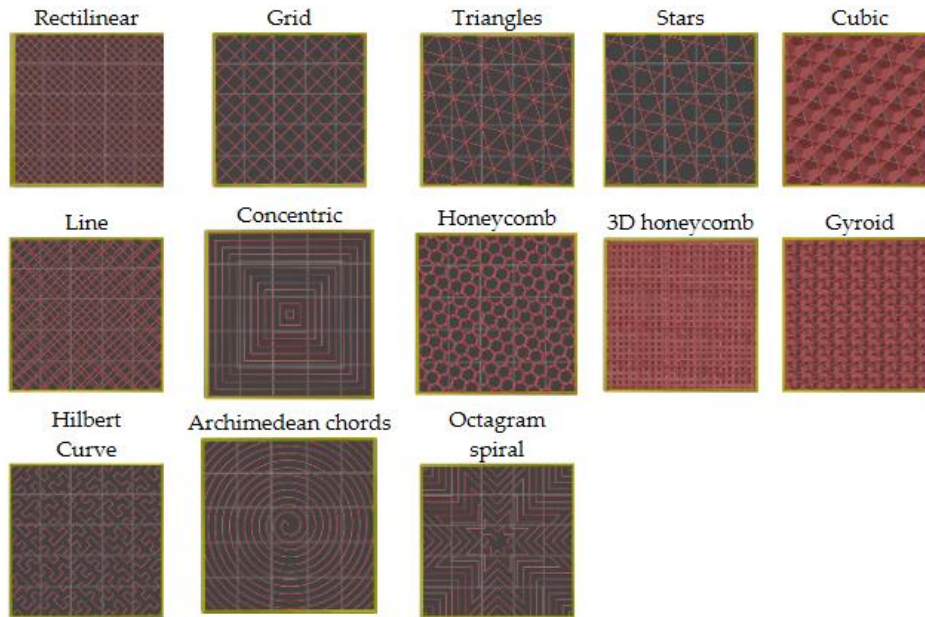


Figure 10: Selectable infill patterns in *Prusa Slicer* [45]

Gyroid is now a widely used pattern for 3D printing. It was originally developed for lightweight construction. Now, however, it is also used because of its unique structure, as shown in Figure 11, and the corresponding good mechanical properties. This pattern is also becoming increasingly important in biomedical engineering research. Many studies are investigating the similarity of the gyroid structure to the natural structure of trabecular bone [46–50].

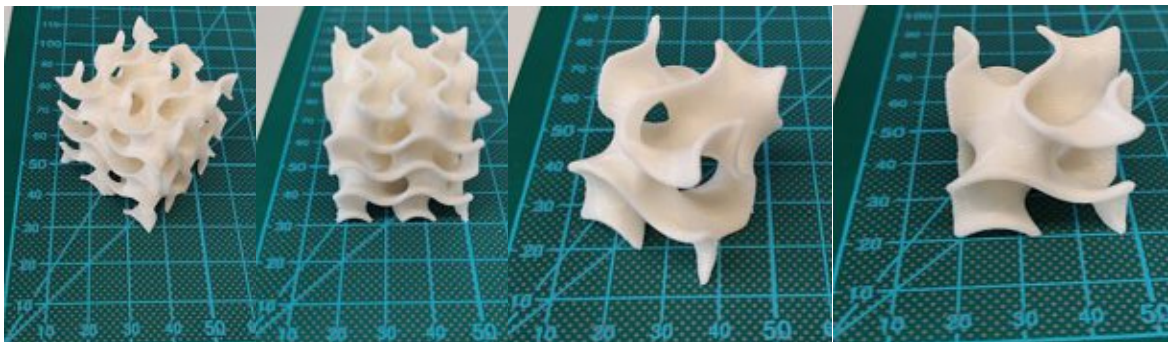


Figure 11: 3D printed *gyroid* structure with zoom in on the right side.

1.7 3D printing in biomedical engineering

3D printing is also being used increasingly in the field of biomedical engineering. Different techniques, which have already been described in chapter 1.6, and different materials are used. Applications range from anatomical models for illustrative purposes to drug delivery and patient-specific implants [51]. In addition, it is possible to carry out biomechanical tests on 3D printed replicas. The FDM technique, as previously mentioned, is simple and cost-effective and for this reason also used in biomedical engineering, for which many studies exist.

In their study, Bartikan et al. [52] printed skull bones based on CT data using the FDM technique. The results show that extrusion-based 3D printing can produce complex models with high detail accuracy. This is also confirmed in the study by Rebong et al [53]. In this study, the accuracy of the prints of dental resin models produced with three different methods (FDM, Polyjet and SLA) was compared. The result of the study by Lee et al. [40] shows an identical result. In this study, the accuracy of the prints of replica teeth, which were produced with FDM and the Polyjet process, was investigated.

The behavior of whole printed bones is also being continuously researched. Thus, Xu et al. [54] investigated the in vitro mechanical behavior of 3D printed goat femora fabricated from CT data using the FDM technique with PCL/ HA material in their study. As a result, the printed bones were found to have similar mechanical properties to the natural bone.

Bone tumors may be a cause of the need for bone replacement, and the in vivo behavior of FDM printed bone is also under continuing investigation. The study by Kang et al. [55] shows that a rib prosthesis made of Polyether Ether Ketone (PEEK), which was manufactured using the FDM technique, could be successfully implanted and closely resembled the mechanical behavior of a natural rib.

1.8 Aim of this work

Currently, artificial bones, such as ORTHObones (3B Scientific GmbH), are often used for bone training purposes. These reproduce the haptics and optics of real bones very well but exhibit a mismatch in the mechanical properties compared to real bones. Artificial bones are also used to validate numerical models or for biomechanical testing. As currently artificial bones represent the real bone in a very simplified way, this should be changed to make the bones more suitable for use. In previous studies it was shown that high accuracy can be achieved with the FDM technique and that this technique is also suitable for reprinting bones. In addition, some studies have shown that the *gyroid* structure can reproduce the trabecular bone quite well in terms of mechanical properties.

The aim of this work is to find out to what extent 3D-printed bones can represent real bones. Therefore, special attention will be paid to the cortical thickness and the accurate bone density dependent infill pattern. First, the influence of simplified visualizations of cortical thickness and bone density will be shown. In the next step, the difference between various femora will be investigated. Finally, a comparison between the 3D printed and the real bones will be made. The 3D prints are based on previously generated QCT data from human donors of three different femora. The verification is done by biomechanical tests using a universal testing machine. In the next step, the achieved maximum load and stiffness of the 3D printed bones will be compared with the experimental data of the real bones on which the 3D prints are based. The workflow of the study is shown in Figure 12 and divided into three categories. In the first step, the obtained QCT data are segmented, and the densities of the trabecular region are mapped. The generated STL files are merged, and the bones are printed. In the second step, the printed bones are proximally and distally embedded and tested on compression. In the third step, the structural properties (max. load and stiffness) are evaluated and compared with each other and with real bones, based on the results represented by Dall'Ara et al. [20].

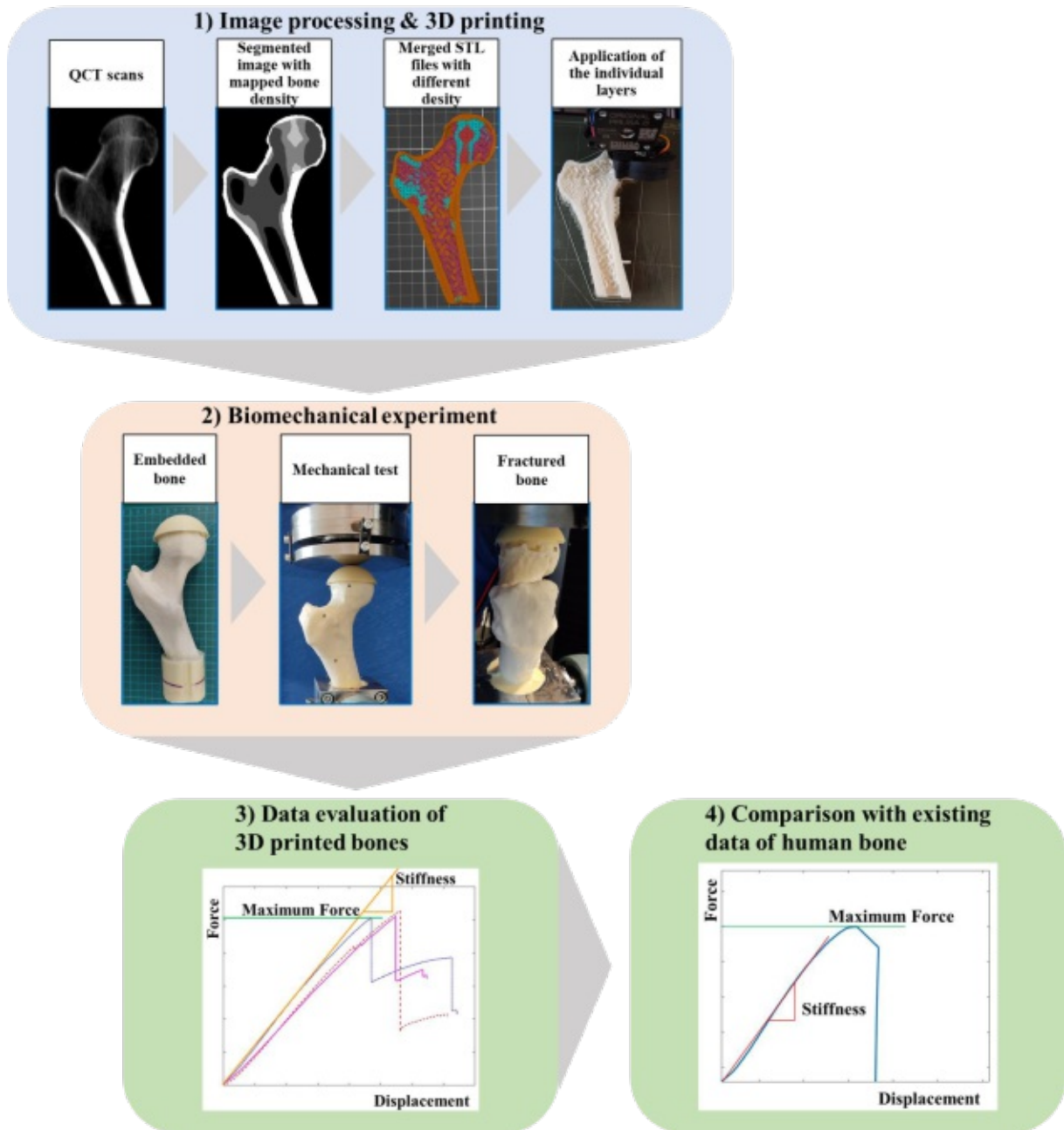


Figure 12: Study design

2 Material and Methods

For this study, the QCT data of three different human femora from a recent study [20] were used, which have different bone densities. These three bones were chosen because they were all tested in the STANCE configuration and two of three cracked at the neck region. In addition, one selection criterion was the obvious difference in total proximal BMD. Experimental data already exist for all three femora and is shown in Table 5, according to the publication of Dall’Ara et al. [20].

For the following, the bone with the highest bone density will be named *Femur 1*, the bone with an intermediate bone density will be named *Femur 2*, and the bone with the lowest density will be named *Femur 3*.

Table 5: Summary of the experimental data of the three femora [20].

	Femur 1	Femur 2	Femur 3
Max. compressive load in kN	13.62	8.57	4.99
Spring Stiffness in kN/mm	7.09	6.86	3.84
Anatomical Side	Right	Right	Left
Fracture mode	Neck	Unknown	Neck

The QCT data represents the bone including the trabecular structure with a relatively high original image resolution (0.33x 0.33x 1.0 mm). This enables the different density ranges to be easily identified and allows to prepare the bone for 3D printing with a very similar structure. The received QCT images of the bones are shifted by 20° to the anatomical axis [20], this angle is kept in the further process, as seen in Figure 13. On the left side in Figure 13, the angles of the load application during a gait cycle are shown as an example, measured by OrthoLoad Lab (Charité, Berlin, Germany). The chosen 20° angle represents the mean load on the femoral head, because the load does not act directly on the anatomical axis.

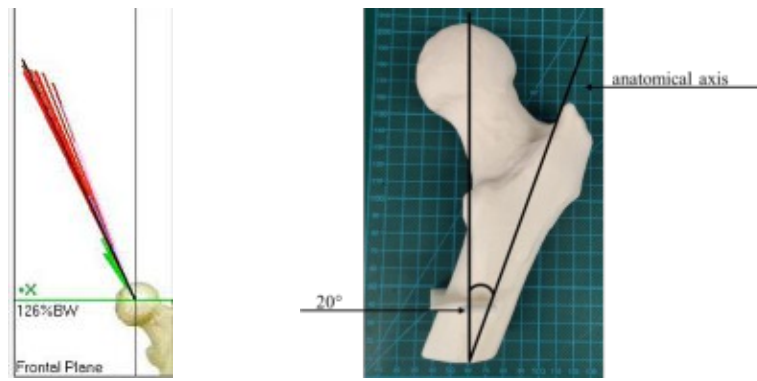


Figure 13: Femur with a displacement of 20° to the anatomical axis. On the left side the force angles during a gait cycle, measured by the OrthoLoad lab (Charité, Berlin, Germany). On the right side the representation of the 20° difference to the anatomical axis.

The aim of this work was to determine the influence of the cortical thickness and the accurate modeling of the bone density on the mechanical behavior. For this reason, three different types were fabricated, differing in cortical thickness and accurate modeling of infill density, as shown in Figure 14. The different colors in the right image represent the different density areas.

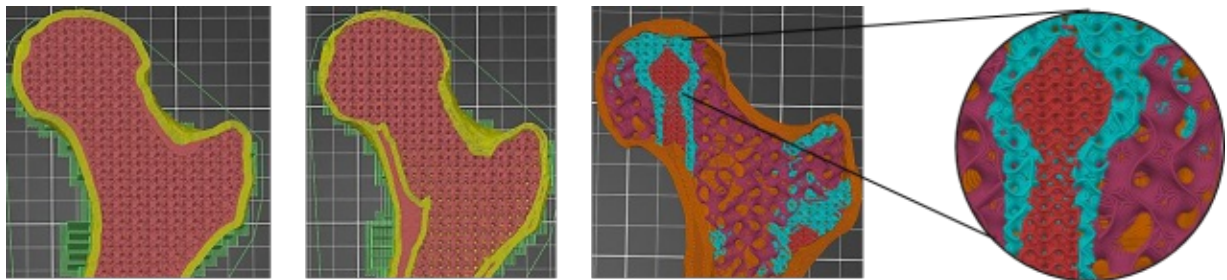


Figure 14: The three different types of one femur. From left to right: Type 1, Type 2, Type 3 with zoom into the various infill densities.

The simplest type is called *Type 1*, with a constant thickness of the cortex and a constant density of the infill and is seen on the far left. *Type 2*, seen in the middle, consists of a variable cortex thickness, but is still characterized by a constant density infill. *Type 3* is the most complex type and has a variable cortex thickness as well as a variable density of the infill. This means that the cancellous bone is packed differently in various areas. All three bone types are shown in Table 6.

For the first part of the study, all three types of *Femur 1* are produced. This represents the comparison of the three different types of one femur. This shows the influence of accurate reproduction of the bone in terms of cortical thickness and infill density. The second part of the study is the comparison of one type of three different femora. *Type 3* is used for this purpose.

Table 6: Summary of the properties of the printed bone types. Each type is printed three times per femur.

	Type 1	Type 2	Type 3
Cortical thickness	Constant	Variable	Variable
Infill density	Constant	Constant	Variable
Printed samples	3	3	3

2.1 Specimen preparation

The anisotropic QCT data contains information about the structure of the bone, such as the thickness of the cortex and the different density regions. All image processing steps are performed with *MedTool* (Version 4.4, Dr. Pahr Ingenieure e.U., Pfaffstätten, Austria).

The first step in this work is to recourse the anisotropic image data with a factor to obtain an isotropic resolution of 1.0x 1.0x 1.0mm for further processing. To ensure that the entire bone is inside the image section, a ten-voxel thick layer with a grey value of zero is generated around the bone. The next step is the segmentation of the bone, which is a complex task. In this work, an automatic threshold followed by a morphological operation is used. The final mask is available from the previous study and had to be improved partially by hand.

Since in this work, as mentioned before, three different types are manufactured, three different image processing procedures were performed. The process of all three types is illustrated in the following Figure 15, whereby each of the three types starts at step one. With higher accuracy of reproduction of the real bones, the number and complexity of image processing steps increases.

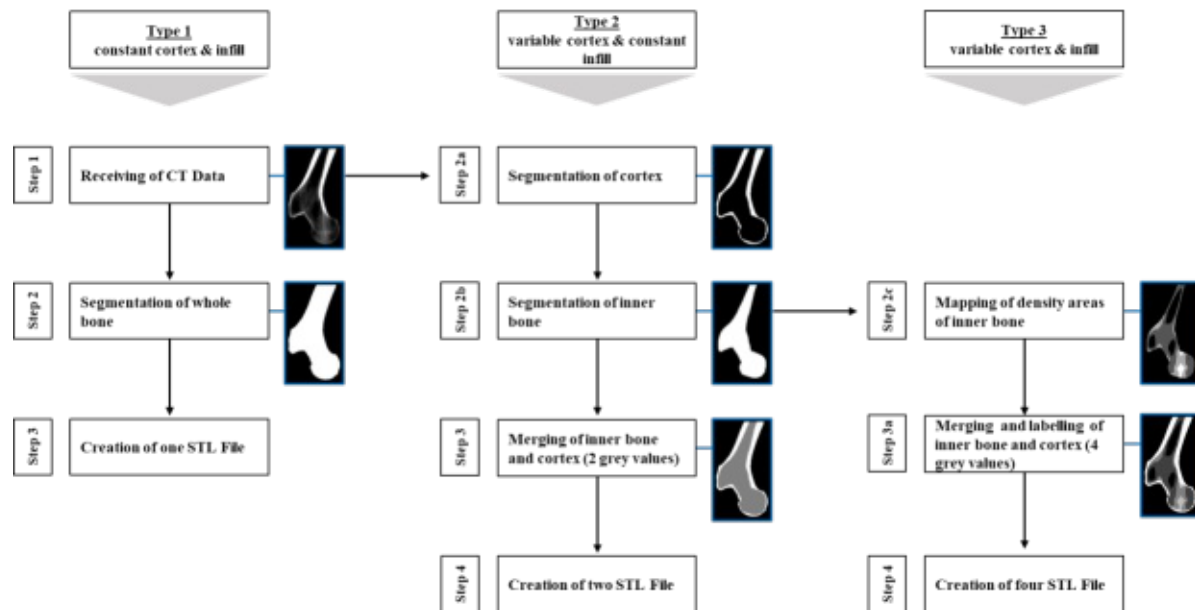


Figure 15: Overview of the process framework of the three types. The pictures show *Femur 1*.

2.1.1 Image processing of Type 1

For this type, the complete bone is segmented with a grey value of one. This is realized by an automatic threshold and a following morphological operation. With the command *-fill pores*, any gaps in the automatic segmentation are closed. Since the cortex and the infill are constant for *Type 1*, only one STL file is created from the segmented bone with *MedTool's Fabricate* – 3D print script. All steps of the procedure of *Type 1* can be seen on the far left of Figure 15.

2.1.2 Image processing of Type 2

In contrast to the first type, the real cortex thickness is reproduced for this type. The trabecular bone has a constant density and a grey value of one, but the thickness of the cortex is considered separately. For this, an automatic threshold is used to represent the contour of the bone which has a grey value of two. In the next step, this contour is subtracted from the segmented bone in Type 1 to depict the trabecular center. Afterwards, the cortex, with a grey value of two, and the cancellous bone, with a grey value of one, are merged, everything around it has the grey value zero, which means air.

Like the first type, STL files can be created with the help of *MedTool's Fabricate* script. Because *Type 2* has a variable cortex and a constant infill, two separate STL files are required, that can be generated by setting *-multi material* option. Thereby the greyscales are used to create the separate STL surfaces.

Calculation of the constant infill density

To be able to use a constant infill density for *Type 1* and *2*, the average density of the trabecular center is calculated. For this purpose, the BMD calibrated grey values were scaled from 0- 1064 mgHA/cc to 0-250 (1 Byte, 255 possible materials) [20] of the trabecular center and summed up. This is done for the trabecular center with a grey value range between zero and 250, as well as for the binary trabecular center with grey values of zero and one as shown in Table 7. The following formula can be used to calculate the average density ρ (in percent) of the trabecular center, where GV_{250} is the sum of the grey values from zero to 250 and GV_B is the sum of the grey values of the binary image.

$$\rho = \frac{\sum GV_{250}}{(250 * \sum GV_B)} \quad (1)$$

Table 7: Sum of grey values and mean density of the trabecular center

	Sum of grey values	Average density in %
Trabecular center with grey values between 0 and 250	$1.74 \cdot 10^{13}$	15,8
Binary trabecular center with values of 0 and 1	$4.41 \cdot 10^{11}$	-

The calculated average density is rounded to 16% and used for the later adjustments of the 3D print.

2.1.3 Image processing of Type 3

This type is also used for comparison between the three different femora. *Type 3* reproduces the different density ranges of the cancellous bone most accurately, based on the QCT images. The cortex is variable here as well and is segmented with an automatic threshold to represent only the contour, as in the previous type.

However, this type is very different from the previous two because the trabecular center does not have a consistent density, rather it is divided into separate areas with different grey value ranges.

For this purpose, *MedTool's CT Interpolator* script is used to compute the individual density regions in the bone. This script does several morphological analyses using the ROIs cropped from the CT images. The application can additionally use interpolation to develop a homogenized material map based on the bone density regions [56], for instance using the power law for isotropic models. More details are published in the paper by Pahr et al. [57]. The calculated values are interpolated for each finite element based on a rectangular background grid, as can be seen in Figure 16. The grey values are mapped to elements and averaged, so the image has the same size as the input image.

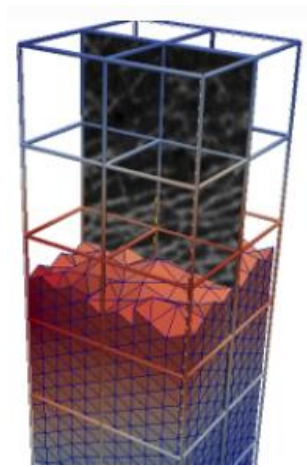


Figure 16: Interpolated computed values based on a background grid [56]

The first step using the *CT Interpolator* script is to set the number of bins. The number of bins is used to calculate the step size in which the individual densities are mapped together. This means that the step size is determined by dividing 100% by the number of bins.

The trabecular centers of all three femora were mapped in three density areas, for which eight bins were used for the first femur and ten bins for the other two, as shown in Table 8. The difference in step size results in a difference in the later adjustment of the infill density for the prints, which is also shown in the following table. It is calculated based on the number of bins with the following formula, where 100 and the step size are in percent and the absolute number of bins are used.

$$\frac{100}{bins} = step\ size \quad (2)$$

The step size is used to determine the infill densities in percent of the mapped areas. For the first region only the step size is used, for the second the step size is multiplied by two and for the third area the step size is multiplied by three.

Table 8: Mapped density areas in relation to the number of bins.

	Femur 1	Femur 2	Femur 3
Number of mapped areas	3	3	3
Number of bins	8	10	10
Infill densities for 3D printing in %	13; 25; 38	10; 20; 30	10; 20; 30

The grey value range of the obtained density map is scaled from zero to three, followed by the labeling of the three ranges, as shown in Figure 17.

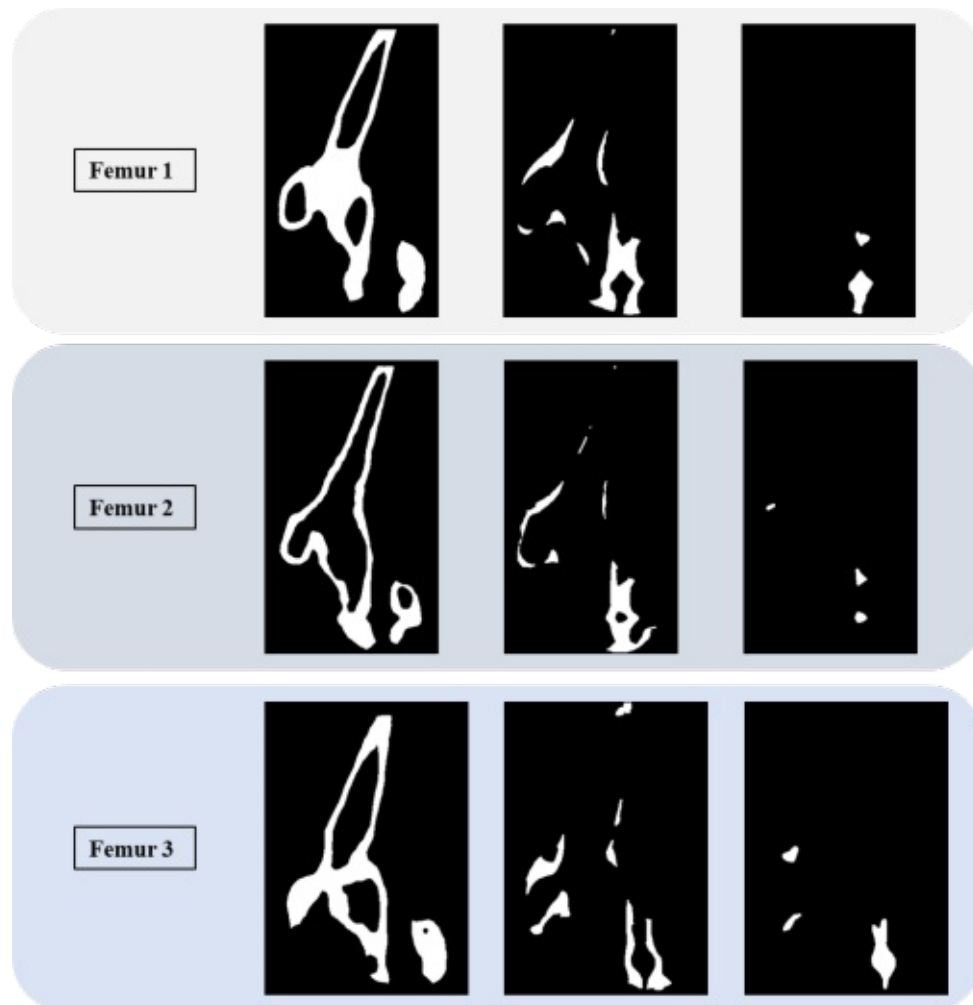


Figure 17: All three femora with the different separated grey values for different densities.

The largest area has the grey value of one, the middle area a value of two and the smallest area a value of three. This is obtained from the generated histograms. These show on the x-axis at which grey value the individual bins are located and on the y-axis the amount of data mapped to this bin. Figure 18 shows the difference of the femora with respect to the individual areas and the histograms.

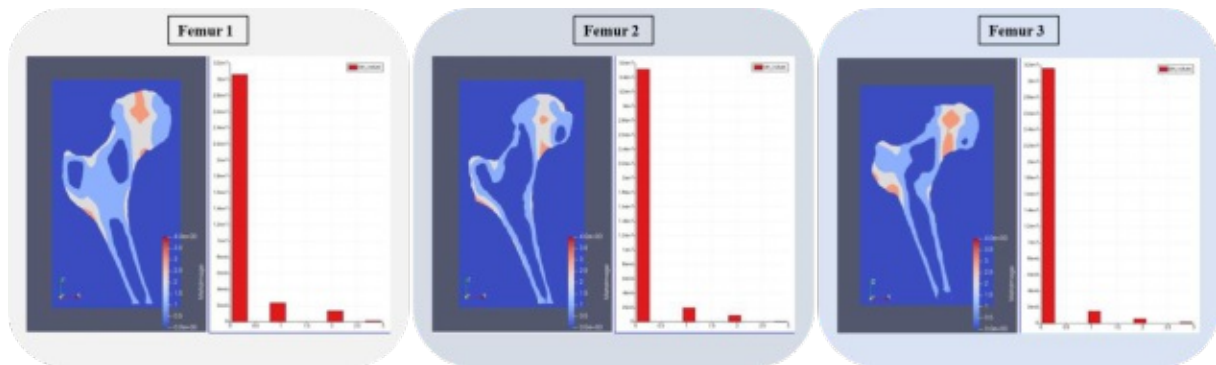


Figure 18: Mapped density areas of the three femora with the resulting histograms.

The used QCT data differ greatly in bone density, this is also clearly seen by the mapping in image processing. Figure 19 shows the three mapped densities, these images here represent a straight cut through the center and thus only illustrate a certain area in the bone. The top section of the figure shows the real bone density distribution, the bottom section shows the areas mapped with the *CT Interpolator*. *Femur 1*, on the very left, is the bone with the highest bone density. *Femur 2*, in the middle, has intermediate bone density, with a lot of air inclusion. *Femur 3* has the lowest bone density, which can be seen mainly at the outer side of the cancellous bone, as shown in Figure 19 on the very right.

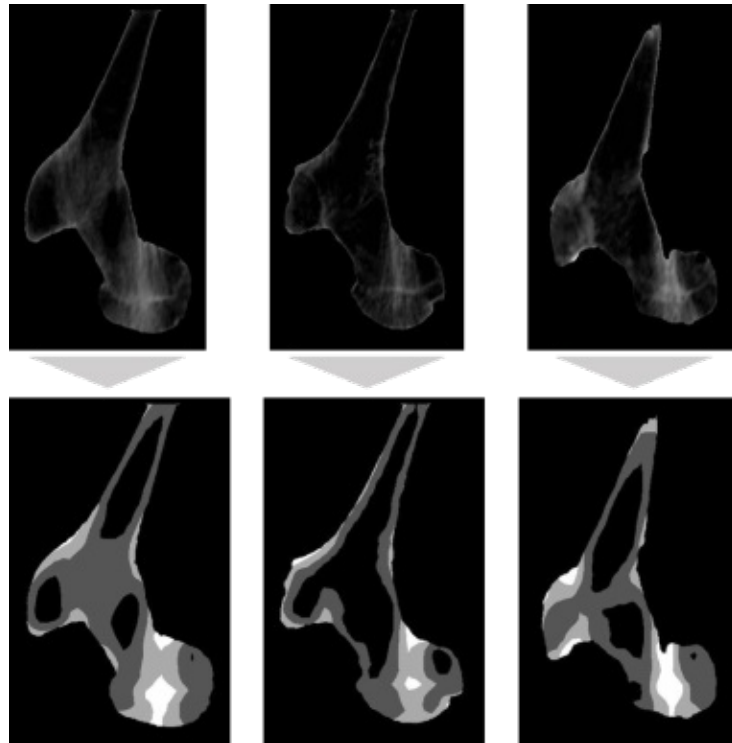


Figure 19: Cross section of the trabecular centers of the three different femora, on top the real density distribution, on the bottom the three resulting density area maps. From left to right: *Femur 1*, *Femur 2*, *Femur 3*

The cortex is then merged with the trabecular center. For *Type 3*, the cortex has a grey value of four. Afterwards, the script *fabricate* is used to generate the STL files. There are four STL files for this type, for each grey value a separate file is generated by setting *-multi material*.

2.2 3D print and the parameters

An original *Prusa* (Prusa Research, Prague, Czech Republic) 3D printer (Model MK3S) was used for printing the bones. This is a cost-efficient printer which melts the material using the FDM method, as described previously in Chapter 1.6, and then applies it layer by layer to the print bed [58]. *Prusa Slicer* (Version 2.1.0, Prusa Research, Prague, Czech Republic) was used for the print setting and the settings of the various parameters. The STL files previously generated in *MedTool* are read into *Prusa Slicer* and prepared for 3D printing and saved as GCODE. This format contains all the important information required by the printer. A separate GCODE is created for each of the three femora and each of the three types.

2.2.1 Used Material

For all bones Prusament PLA Vanilla White (Prusa Research, Prague, Czech Republic) was used. The material has been described previously in chapter 1.6.1, it was selected because of its low price, because it is a high strength and high modulus polymer, and because it is an easily printable material [44]. Table 9 shows the most important print properties of this material according to the manufacturer's specifications.

Table 9: Properties of PLA vanilla white according to the technical sheet [44].

Name	Chemical name	Diameter in mm	Density in g/cm ³	T _{Nozzle} in °C	T _{Heat Bed} in °C
PLA	Polylactic Acid	1,75 ± 0,02	1,24	210 ± 10	40 – 60

2.2.2 Editing of the three types for 3D printing

To ensure consistent alignment of all bones for the further process, a spacer was printed directly onto the bones, which is shown in Figure 20. The spacer is located in the same position on all femora and all types and was designed with *SolidWorks* (Version 2019, Dessault Systèmes, Vélizy-Villacoublay, France). The spacer is adapted to the bone in *Prusa Slicer* and has the following dimensions for all femora: length: 62.5mm, width: 30mm, depth: 2mm. Printed with three top and bottom layers and three perimeters with 100% rectilinear pattern, it can be easily removed after alignment.

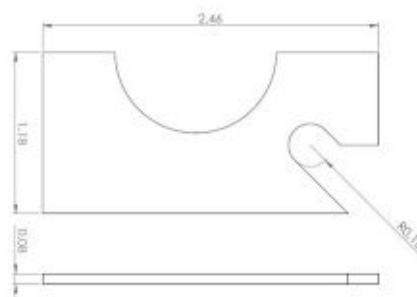


Figure 20: Technical drawing of the spacer with a hole for the alignment.

Based on a previous test, with the results in the Appendix A, all specimens are printed horizontally, as therefore, the printed fibers are aligned along the direction of the subsequent force impact. To realize this, support material with an overhang angle of 55° and the rectilinear pattern is required on the build plate, which is easy to remove. As PLA is used for printing, the

extruder temperature is set to 220°C and the bed temperature to 60°C for all femora, as recommended by the manufacturer.

As already discussed in chapter 1.6.2, the *gyroid* structure can represent the trabecular bone in a good way. A previous study has shown that with increasing infill density, the strength also increases. In addition, it was found that up to an infill density of 20%, the print direction has no influence on the elastic modulus and the strength. Despite the complex 3D structure, the printing time is not greatly increased compared to other types of infill.

The layer height used in this work is 0.3mm. Due to the geometry of the bone, the printing time would be quite high with a smaller layer height, as it can be determined approximately with the following formula, where t describes the print time and h the layer height.

$$t \sim \frac{1}{h} \quad (3)$$

By choosing a larger layer height, it implies that there is a smaller number of layers and the material is melted for a longer time. Statistically, the probability of artifacts is lower with a smaller number of layers.

The extrusion width defines the width of the material that the nozzle of the 3D printer extrudes. The nozzle used here is 0.4mm wide. For this study an extrusion width of 0.5mm was set. The first layer has a smaller extrusion width of 0.42mm to generate a better bed adhesion. The pressure in the nozzle is higher if the extrusion width is larger than the width of the nozzle, because the material has to be pressed to the side after leaving the nozzle. This pressure has the additional effect that the individual layers are squeezed together more tightly.

The default settings of *Prusa Slicer* were used for all other parameters.

 Print settings of Type 1

Since *Type 1*, as previously mentioned, has a constant cortex and infill, there is only one STL file. To set the thickness of the cortex correctly in *Prusa Slicer*, the average thickness of the bone is calculated beforehand.

The average thickness t in mm can be calculated with the following formula, where V is the volume in mm^3 and S is the surface in mm^2 .

$$t = \frac{V}{S} \quad (4)$$

By using *SolidWorks* the volume and surface area of the entire femur can be indicated. Table 10 shows the volume and surface of *Type 1* and the volume of the trabecular center of *Type 2*.

Table 10: Indicated values of the volume and the surface from the 3D Tool for Femur 1 and the infill of Femur 2.

	Type 1	Type 2 Infill
Volume in mm^3	266248.3	161217.0
Surface in mm^2	29445.9	-

The volume of the cortex V_{Cortex} can be determined with the following formula, where V_1 is the total volume of *Type 1* and V_{Infill} is the volume of the infill of *Type 2*, all in mm^3 .

$$V_{\text{Cortex}} = V_1 - V_{\text{Infill}2} \quad (5)$$

All calculated values can be seen in Table 11. With the obtained volume of the cortex V_{Cortex} , the average thickness t is then calculated analogously with the previously described formula (4):

$$t = \frac{V_{\text{Cortex}}}{S_1} \quad (6)$$

Since the printed layer height is 0.3mm, the next step is to calculate the number of top and bottom layers with the following formula, where x is the number of top and bottom layers, t is the average thickness of the cortex and h is the layer height, both in mm.

$$x = \frac{t}{h} \quad (7)$$

The number of perimeters also has a direct influence on the strength. An increased number of perimeters results in an increase of the strength. For *Type 1* of this study, the number of perimeters is set to seven to create a stable shell wall together with the top and bottom layers. The perimeter p was calculated using the following formula, where t is the mean thickness in mm and w is the extrusion width in mm.

$$p = \frac{t}{w} \quad (8)$$

Table 11: Calculated parameters for the settings

	V_{Cortex} in mm^3	t in mm	x (number top & bottom layers)	p (number of perimeters)
Calculated values	105031.3	3.6	12	7.2

As the infill is constant, it is set to 16% *gyroid*, as calculated in chapter 2.1.2. Figure 21 shows the sliced bone with the previously defined parameters in *Prusa Slicer*.

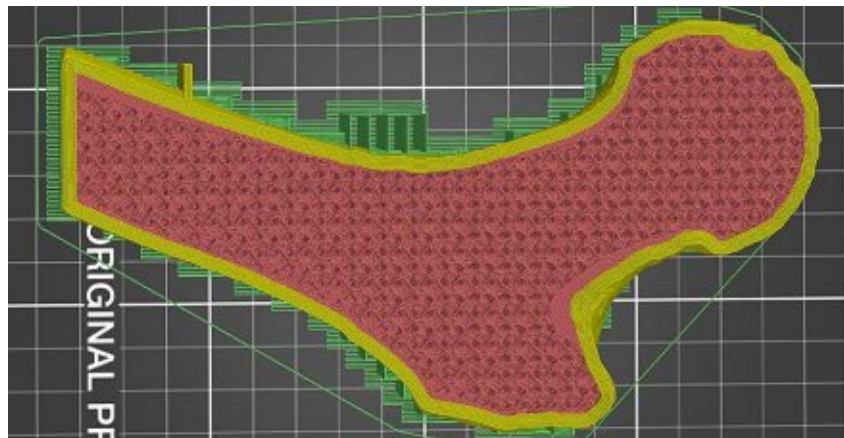


Figure 21: Femur 1 Type 1 with 16% gyroid infill and constant cortex

Print settings of Type 2

Since this type has a variable cortex and a constant infill, there are two STL files that are read and merged into *Prusa Slicer*, as can be seen on the left side in Figure 22. Each STL file can be individually modified in *Prusa Slicer*, which allows different settings for the cortex and the infill. Since the infill is constant for *Type 2*, 16% *gyroid* is chosen as before. Perimeter, as well as top and bottom layers are set to zero for the infill, since the cortex forms the outer shell. The cortex, on the other hand, is variable in this type, so the thickness differs in various regions, and is supposed to represent the thickness of the real bone, which can be seen in Figure 22 on the right. The number of perimeters and top and bottom layers here is five. These settings were chosen in order to reproduce the cortex as real as possible and simultaneously provide conditions for good mechanical properties.

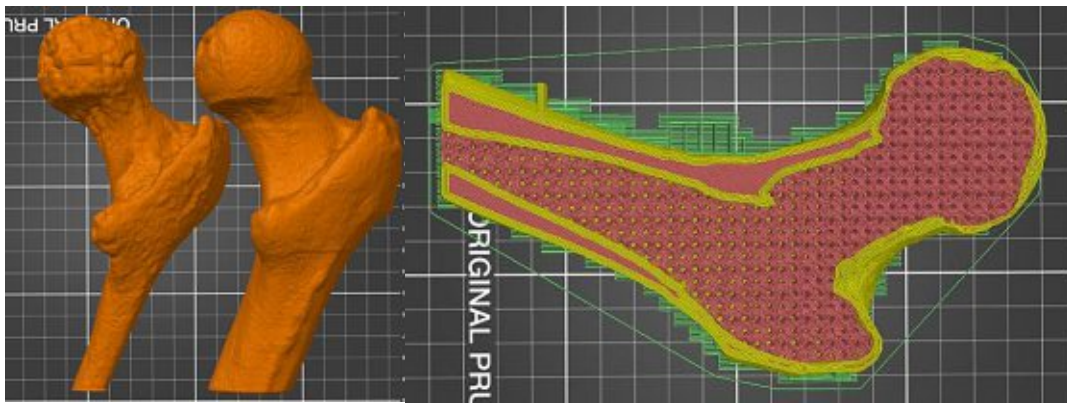


Figure 22: Left: Infill (left) and cortex (right) of *Femur 1 Type 2*; Right: *Femur 1 Type 2* with 16% *gyroid* infill and variable cortex.

Print settings of Type 3

The third type is composed of four STL files, where one STL file is the cortex and three STL files make up the infill. Each STL file of the infill shows a density area previously mapped in *MedTool*. Analogous to *Type 2*, all STL files are loaded and merged in *Prusa Slicer*, as shown in Figure 23. Each color represents a density area and one color represents the cortex.

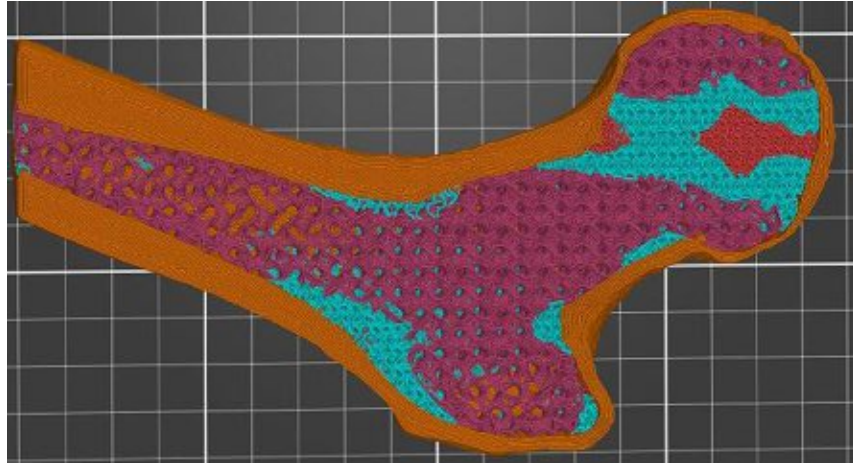


Figure 23: Three infill regions and the cortex of *Femur 1 Type 3*.

The cortex is variable for this type and the settings of the top and bottom layers as well as those of the perimeter can be transferred from *Type 2*. The files of the infill are edited separately. The densities of the areas are based on the step size previously determined in *MedTool*. The histograms in chapter 2.1.3 additionally match the size of the STL to the density. The three infill densities are shown on the far right in Table 12.

The three types of *Femur 1* were compared in the first part of this study, Table 12 shows an overview of the settings made in *Prusa Slicer*. All other parameters which are not listed here are standard settings recommended for the material and the layer height.

Table 12: Settings of the three types of *Femur 1*.

Settings	Type 1	Type 2	Type 3
Layer height in mm	0.3	0.3	0.3
Perimeters cortex	7	5	5
Top & bottom layers cortex	12	5	5
Cortex pattern and density	-	100% rectilinear	100% rectilinear
1. Infill pattern and density	16% gyroid	16% gyroid	13% gyroid
2. Infill pattern and density	-	-	25% gyroid
3. Infill pattern and density	-	-	38% gyroid

Print settings of Femur 2 and 3

The second part of the study is the comparison of *Type 3* of the three different femora, because it reproduces the real bone most accurately. The procedure for choosing the settings is the same as for *Femur 1* in *Prusa Slicer*. The only difference is the infill density, because a step size of ten was chosen in *MedTool* for *Femur 2* and 3. The number of top and bottom layers as well as the number of perimeters is the same as for *Femur 1*. In Figure 24, both sliced bones are shown. All parameters are shown in Table 13.

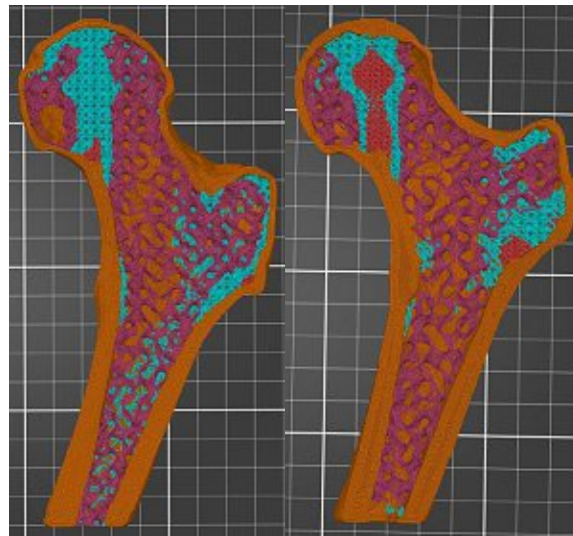


Figure 24: Left: *Femur 2 Type 3* with three differently mapped density areas and a variable cortex. Right: *Femur 3 Type 3* with three differently mapped density areas and a variable cortex.

Because the third type of all three femora will be compared with each other in the further procedure, the respective print settings are summarized in Table 13, where the only difference is the infill density.

Table 13: Settings of *Type 3* of all femora

Settings	Femur 1 Type 3	Femur 2 Type 3	Femur 3 Type 3
Layer height in mm	0,3	0,3	0,3
Perimeters cortex	5	5	5
Top & bottom layers cortex	5	5	5
Cortex pattern and density	100% rectilinear	100% rectilinear	100% rectilinear
1. Infill pattern and density	13% gyroid	10% gyroid	10% gyroid
2. Infill pattern and density	25% gyroid	20% gyroid	20% gyroid
3. Infill pattern and density	38% gyroid	30% gyroid	30% gyroid

2.2.3 Printing process

After the settings have been set in *Prusa Slicer*, a GCODE containing all this information is generated and read into the printer. As the individual types differ in complexity and the femora have varying densities, the printing times and the used filament also differ, as shown in Table 14. The time and used filament shown here is the pure printing time of the bone and the material used only for the bone, without spacer and support material.

Table 14: Summary of the print time and used filament of all femora.

	Femur 1 Type 1	Femur 1 Type 2	Femur 1 Type 3	Femur 2 Type 3	Femur 3 Type 3
Print time	8h 16min	9h 38min	10h 56min	8h 21min	7 h 13 min
Used filament in m	55.07	54.06	54.20	39.23	34.65
Number	3	3	3	3	3

The alignment on the print bed was consistent for all bones. For good reproducibility, each of the bones was printed three times. Figure 25 shows *Type 1* and *2* of *Femur 1* during the printing process and the printed infill of the two bones.

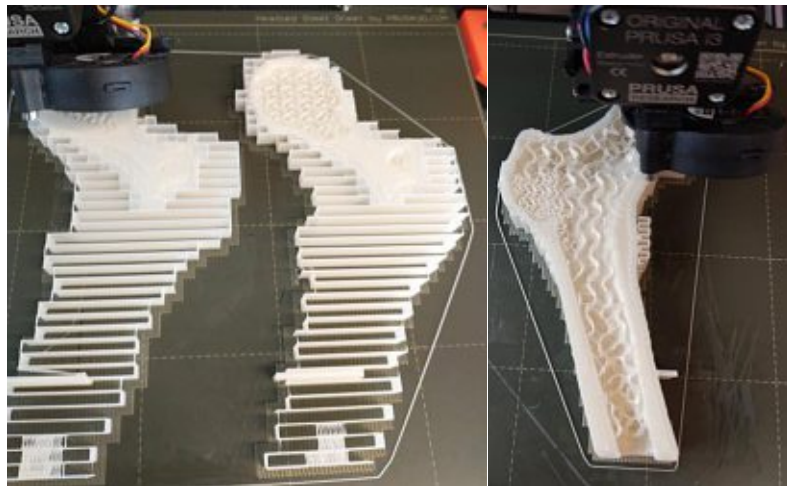


Figure 25: *Femur 1* Type 1 & 2 during the printing process and right the infill of *Femur 3* Type 3.

After completing the print, the support structure was carefully removed, and the bones were weighed. This measurement is used to verify the print. Since each bone was printed three times, this is to confirm that all bones of one femur or type have a comparable mass. Table 15 shows the calculated weight of the femora with *Prusa Slicer* and the mean value with standard deviation (SD) of the measured weight.

Table 15: Comparison of calculated weight from *Prusa Slicer* and mean value of measured weight with standard deviation.

	Average measured weight in g with SD	Calculated weight in g
Femur 1 Type 1	152.33 ± 1.70	164.24
Femur 1 Type 2	149.00 ± 0.82	161.25
Femur 1 Type 3	148.33 ± 2.36	161.67
Femur 2 Type 3	113.67 ± 0.47	117.01
Femur 3 Type 3	100.00 ± 0.00	103.34

2.2.4 Post processing

In a previous test, it was discovered that it is necessary to saw off a piece of the shaft so that the femur can be aligned flat in the embedding tool. Additionally, in this test, found in the Appendix, it was observed that both the shaft and the head must be embedded to achieve good results.

After removing the support structure, one edge of the shaft was removed by hand using a saw, as can be seen in the middle and in the right picture in Figure 26. For this purpose, the bones were always clamped in the same position in the vice, which can be seen in the far left in Figure 26. This was done in order to center the bone in the embedding tool.

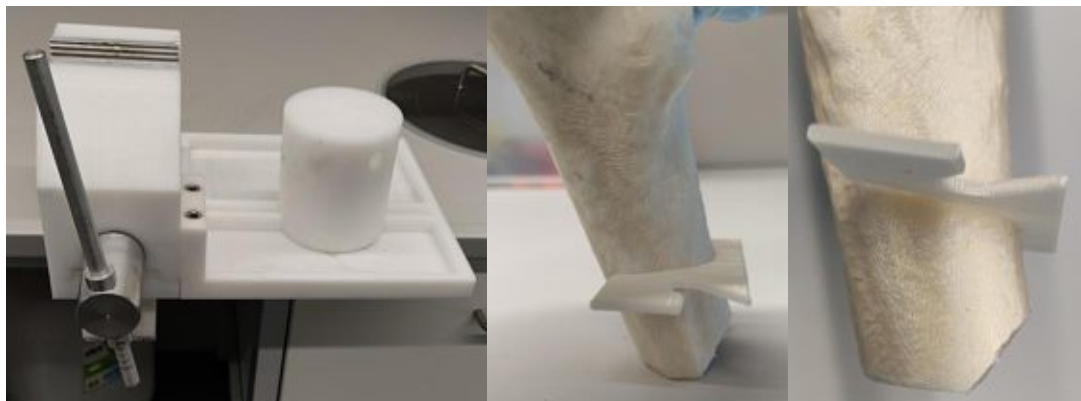


Figure 26: Left: Used vice needed to remove an edge of the bones. Middle and right: Removed edge of the shaft.

The result of embedding the bone is that the force absorption is constant, the shaft was embedded first, the embedding tool can be seen on the far left in Figure 28. 27mm of the most distal part of the femur were embedded with polyurethane (FDW Handelsgesellschaft mbH, Lienzen, Austria). The printed spacer has all femora aligned in the same position on the embedding tool, as seen in Figure 27.

The material used for embedding is a 50:50 mixture of resin and hardener (PUR145 and SG141/4), of the polyurethane, which was freshly mixed for each embedding process. To achieve good strength, the two-component resin has to harden for a short period of time after pouring.

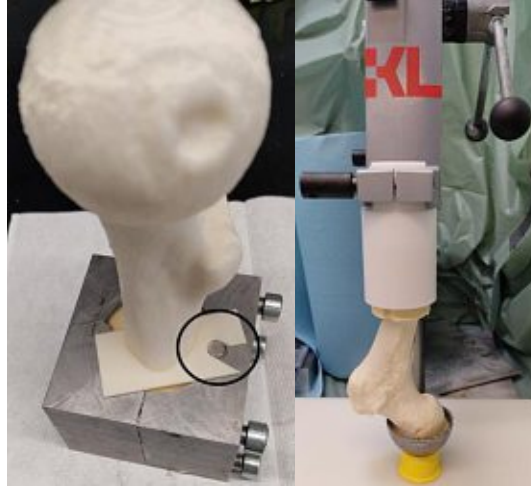


Figure 27: Left: Aligned and embedded femur. Right: Femur in drill stand with embedding of the head.

To embed the head, the bone was clamped in a drill stand using a special tool, which can be seen in the middle in Figure 28. Thus, all bones have the same starting position.



Figure 28: Tool for embedding of the shaft on the left and turned fixture and the cups for the embedding of the head on the right.

A cup, seen on the right in Figure 28, was used for embedding the head in which the bone has about 20 mm all-round space. Since the entire head should not be embedded in this study, as this can lead to false results, a notch was milled into the cups. This ensured the same embedding of the head for all bones. Because the femora have different head diameters, a smaller cup had to be used for *Femur 3*. The right side of Figure 27 shows how the bone is clamped in the drill stand and the head is embedded with 20 mm. Previously, the cup was aligned with a level at 0° in all directions. The bone embedded at the top and bottom can be seen in Figure 29.



Figure 29: Embedded femur at the top and bottom.

Before and after embedding, the total height of the bones was measured; this varies very little per femur. Hence, the embedding is consistent at the top and bottom and the condition is the same for each individual bone. Recording this data ensures that any differences in the results of the mechanical tests are not due to post processing. Head and shaft diameters and total height before embedding were measured at the locations shown in Figure 30.

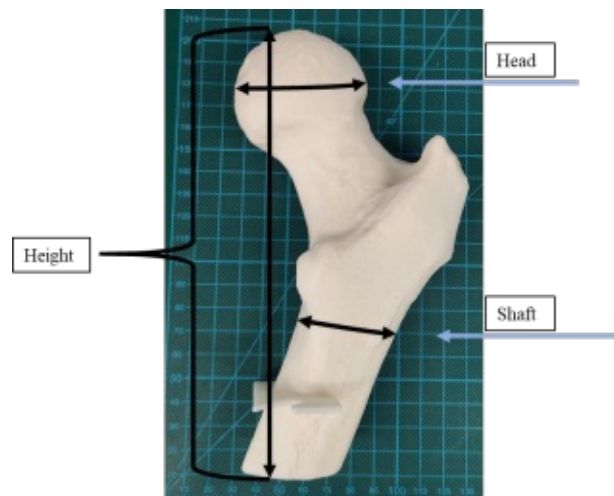


Figure 30: Measuring points of the bone for example on *Femur 1 Type 1*.

Table 16 shows the measured data for all three types of *Femur 1* for all test series. The data of *Femur 2* and *Femur 3* were measured analogously to *Femur 1* and can be seen in Table 16 as well.

Table 16: Details of the three types of *Femur 1* for all three test series, as well as for *Type 3* of *Femur 2* and *3*.

	Femur 1	Femur 1	Femur 1	Femur 2	Femur 3
	Type 1	Type 2	Type 3	Type 3	Type 3
Diameter shaft in mm	34	34	34	30	29
Diameter head in mm	54	54	54	51	45,5
Height w/o embedding in mm Test 1	173	173	172	170	152
Height w/o embedding in mm Test 2	170	171	170	170	152
Height w/o embedding in mm Test 3	172	172	172	170	152
Height w/ embedding in mm Test 1	198	198	196	198	179
Height w/ embedding in mm Test 2	198	198	198	197	180
Height w/ embedding in mm Test 3	198	198	197	198	179

2.3 Mechanical testing

After preparation, the specimens were clamped in the mechanical testing machine *Zwick Roell Z030* (Zwick Roell GmbH & Co. KG, Ulm, Germany) with pneumatic clamps to perform uniaxial compression tests in the STANCE configuration. All compression tests were carried out with the same machine and the experimental data were recorded with the *testXpert II* (Zwick Roell GmbH & Co. KG, Ulm, Germany) software [59]. There was a constant room temperature and humidity during the performance of all tests. For *Femur 1*, all three types were tested serially on each of three days. *Femur 2* and *3* were tested on different days in each case.

The specimens were fixed with the shaft in the tool originally used for embedding in order to simulate a one-legged STANCE configuration of the femur. Since the obtained QCT data already have an angle of 20° with respect to the proximal shaft and since this is required for testing the STANCE configuration, the bones were clamped straight in the machine. For all bones, the load was applied on the femoral head, as seen in Figure 31. The entire assembly of specimen and distal tool was manually aligned along the loading axis of the machine using a level and a laser.

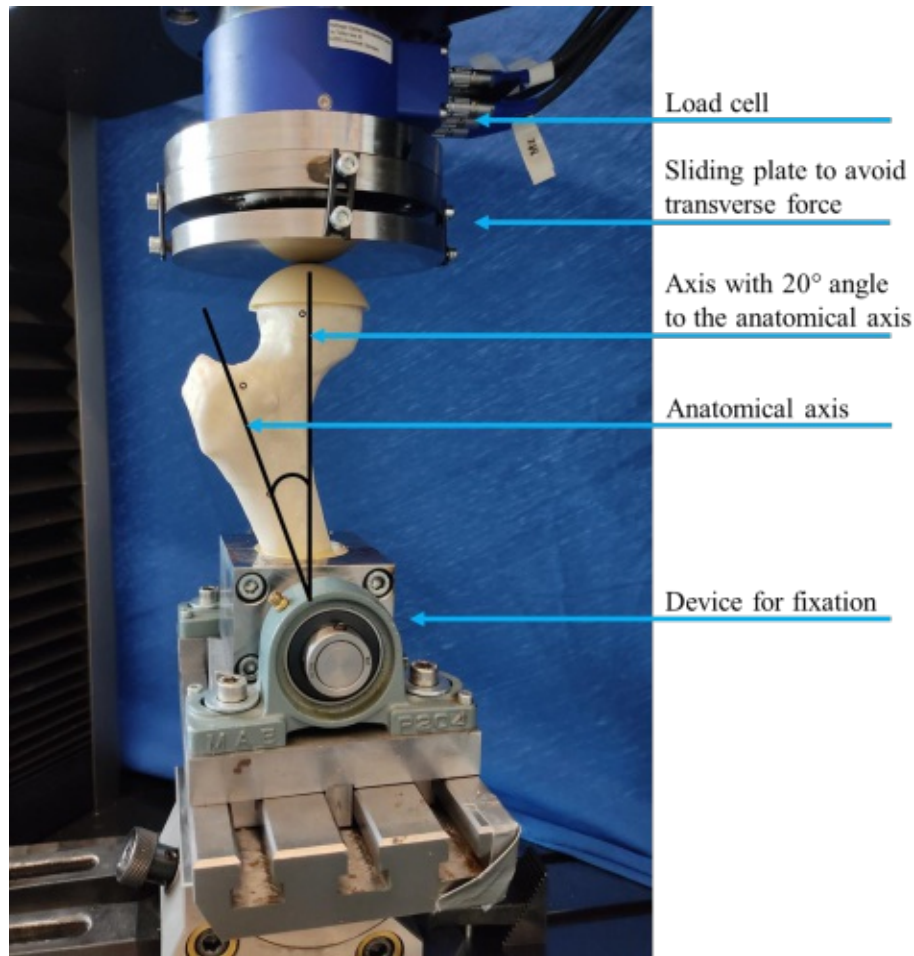


Figure 31: Experimental setup for STANCE configuration of the femur.

The test was position controlled with 5mm/min and a standard travel of 30mm without preload. Force and displacement were recorded during the test, at 100Hz with a 25kN load cell (HBM MCS10, HBM GmbH, Darmstadt, Germany) and transferred via the data acquisition module *HBM QuantumX* (HBM GmbH, Darmstadt, Germany) to the *testXpert II* software. The tests were stopped manually after failure. The recorded displacement in this study does not represent the actual displacement of the bone, only the machine displacement is recorded.

2.4 Data analysis and processing

The maximum force was defined as the maximum compressive load that the bone can resist. The stiffness was determined as the slope of the linear part of the recorded load-displacement curve, schematically shown in Figure 32. As testing was done without preload, the data was modified to start at 0mm displacement.

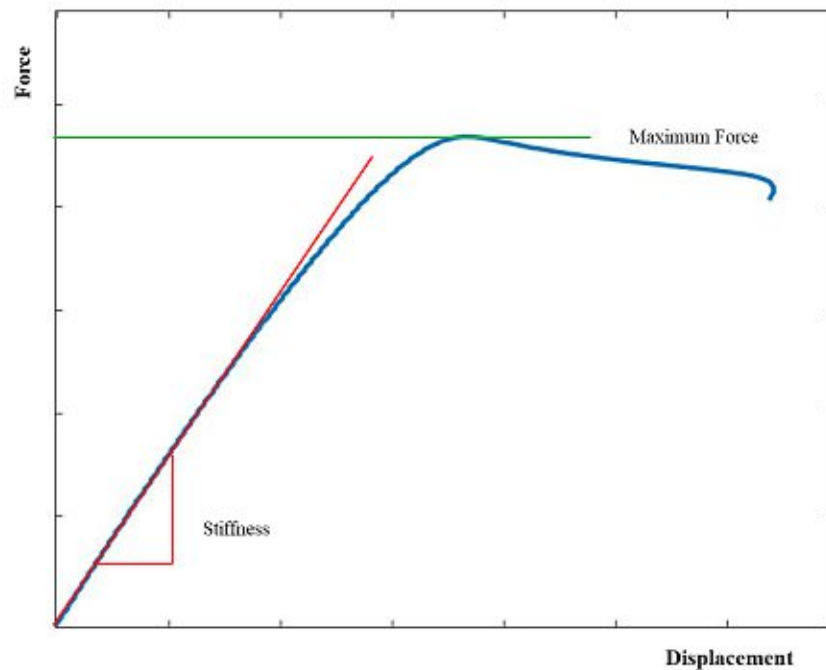


Figure 32: Schematic load- displacement curve for a bone, where F is load and d is displacement. The stiffness is calculated from the linear region.

For all bones, the values of 300N and 600N were used to apply the following equation and calculate the stiffness K in N/mm, where F is the force in N and L is the displacement in mm.

$$K = \frac{\Delta F}{\Delta L} \quad (9)$$

The spring stiffness K is calculated from a load displacement curve. This describes the extrinsic properties of the bone, referring to the structure. The stiffness can be defined as the resistance against deformation. When considering the Young's modulus, this is obtained from the stress-strain diagram, in the same way as the stiffness, but the Young's modulus describes the intrinsic properties of the bone, i.e. the material itself [60].

One diagram for each femur and type is created and an additional diagram is created with the mean values of *Type 3*. The mean values are calculated using the arithmetic mean with the following formula, where \bar{x} is the arithmetic mean, n is the number of values, and x_i is the values.

$$\bar{x} = \frac{1}{n} \sum_{i=1}^n x_i \quad (10)$$

For every mean value, the standard deviation s was calculated using the following formula, where n is the number of values, \bar{x} is the arithmetic mean and x_i is the values.

$$s = \sqrt{\frac{1}{n-1} \sum_{i=1}^n (x_i - \bar{x})^2} \quad (11)$$

The empirical coefficient of variation was used to show the accuracy of reproducibility. Which is a dispersion from the mean value in percent. The following formula was used to calculate the coefficient of variation v , where s is the standard deviation and \bar{x} is the mean value.

$$v = \frac{s}{\bar{x}} * 100\% \quad (12)$$

3 Results

In total fifteen femora were tested successfully in the biomechanical experiments. They were all fabricated using the FDM 3D printer, tested in STANCE configuration and a load-displacement curve was recorded and further evaluated with *MATLAB* (Version R2020b, MathWorks, Natick, USA). The results of the ultimate force and stiffness as well as their comparison are presented in the following sections. First, the influence of a simplified cortical thickness and constant bone density will be shown. In the next section, the difference between different femur types will be investigated. Finally, a comparison between the 3D printed and the real bones will be made. In addition, a qualitative description of the fracture modes observed in the experiments is given. For *Femur 1*, three different types (Type 1- 3) were tested, whereas for *Femur 2* and 3 only *Type 3* was tested. Each bone or type was printed three times, which is described as Test 1- 3 in the following, in order to investigate the reproducibility of the 3D printed bones.

3.1 Influence of reproduction accuracy

To evaluate the influence of reproducibility accuracy, each type of any bone was printed and tested three times. This chapter presented the results of the test set of *Femur 1 Type 3*, the results of the other types and bones can be found in the Appendix A.

Figure 33 shows the load- displacement curve of the test set of *Type 3* for *Femur 1*. The course of the three tests is almost identical, so the difference in stiffness is small, but the difference in the maximum force is more noticeable. Test 1 reaches the highest maximum force, test 2 and 3 are in a similar range for maximum force. Test 3 has multiple small pre-breaks before reaching the maximum force, while test 1 has one pre-break and reaches the highest maximum force afterwards.

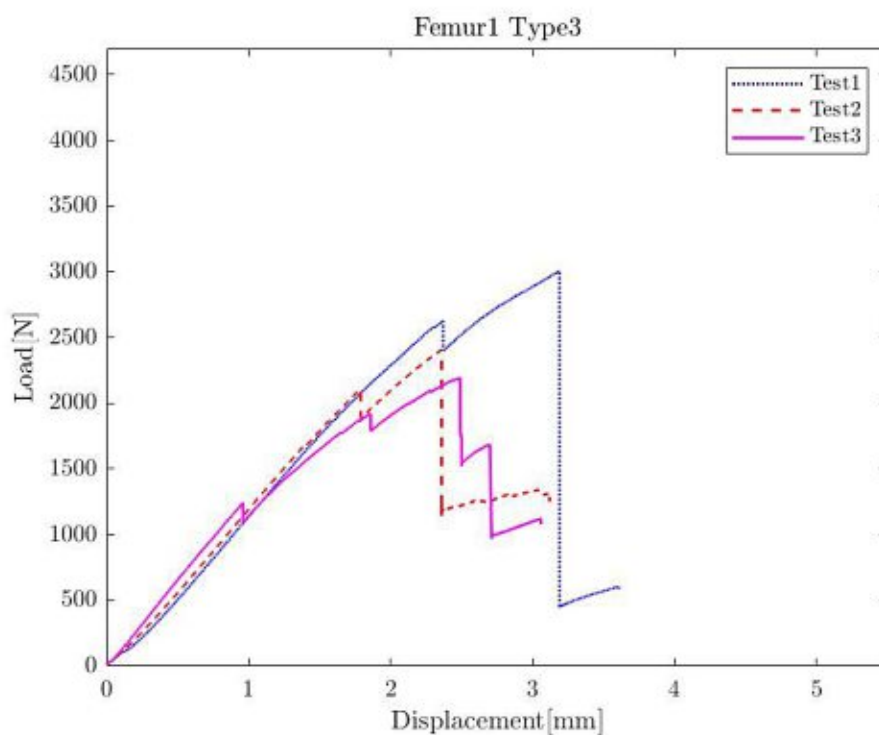


Figure 33: Results of the test set of Type 3 of Femur 1.

Table 17 shows the maximum force, as well as the stiffness for all three tests of *Femur 1 Type 3*. Test 3 had the lowest maximum force, but the highest stiffness.

Table 17: Maximum force and stiffness of the test set of Type 3 of Femur 1.

	Max. force in N	Stiffness in N/mm
Test 1	3006.17	1201
Test 2	2405.96	1249
Test 3	2193.79	1364

As shown in Figure 34 the fracture points of test 2 and test 3 are very similar and show a splitting of the head. By visual inspection, these can be classified as head fractures. In contrast, the fracture point of test 1 is located more in the direction of the neck in the front and additionally has a fracture on the head on the back side. This fracture can be classified as a simple transcervical neck fracture.



Figure 34: *Type 3* of *Femur 1* of all test runs, from left to right: test 1, test 2, test 3.

3.2 Influence of different printing types

To identify the influence of accurate mapping of cortical thickness and infill density, the different types of *Femur 1* were tested and are presented in this chapter. Figure 35 shows the load displacement curve of the selected three types, the results of the individual test runs can be found in the Appendix A. *Type 1*, with a constant cortex and a constant infill, shows a high maximum force. *Type 2*, with variable thickness and constant infill, has the lowest maximum force. The max. force of *Type 3*, with variable thickness and variable infill, is in between the other two types.

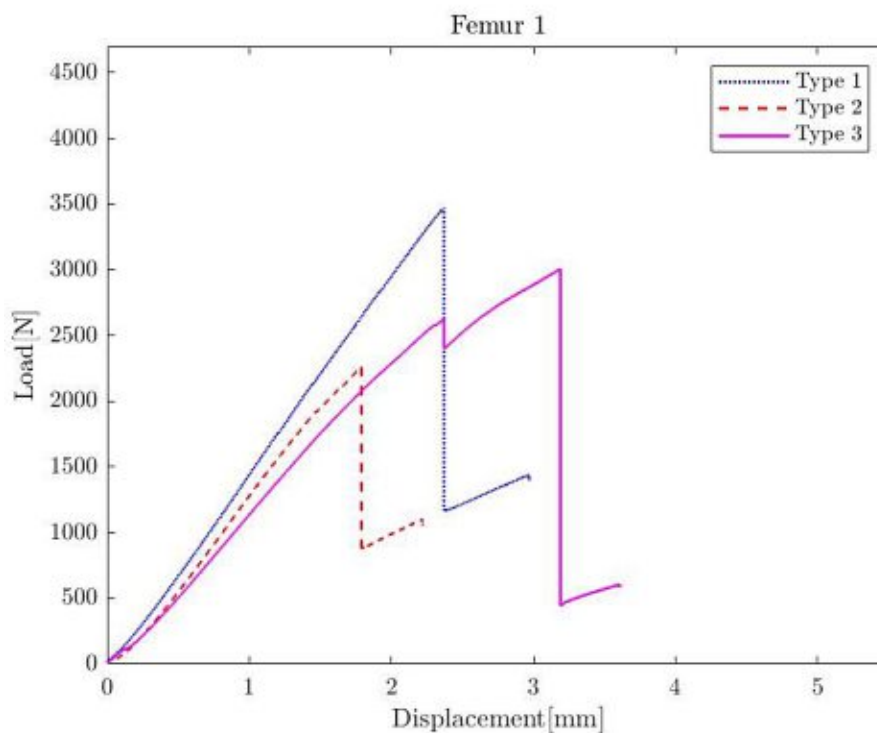


Figure 35: Results of *Femur 1* for the selected three different 3D printing types.

Table 18 shows the minimum and maximum value, as well as the mean value with standard deviation (SD) of the ultimate force and stiffness for all three types of *Femur 1*, calculated with the formulas described in chapter 2.4.

Table 18: Maximum force and stiffness of all types of *Femur 1* with the mean value with standard deviation.

	Min.	Max.	Mean with SD
Type 1 max. force in N	3471.31	4515.30	3936 ± 434
Type 1 stiffness in N/mm	1363	1502	1454 ± 65
Type 2 max. force in N	2262.52	2459.72	2336 ± 88
Type 2 stiffness in N/mm	1246	1362	1285 ± 54
Type 3 max. force in N	2193.79	3006.17	2535 ± 344
Type 3 stiffness in N/mm	1201	1364	1271 ± 68

As shown in Figure 36, *Type 1* and *2* split in the middle of the femoral head by splitting. *Type 3* also cracks at the head, but the fracture extends to the neck. All of the fractures are artificial fractures caused by layer splitting and, therefore can not be classified by AO classifications.

However, since *Type 1* does not realistically represent a real bone with the different density regions, only *Type 3* was produced for *Femur 2* and *3*.

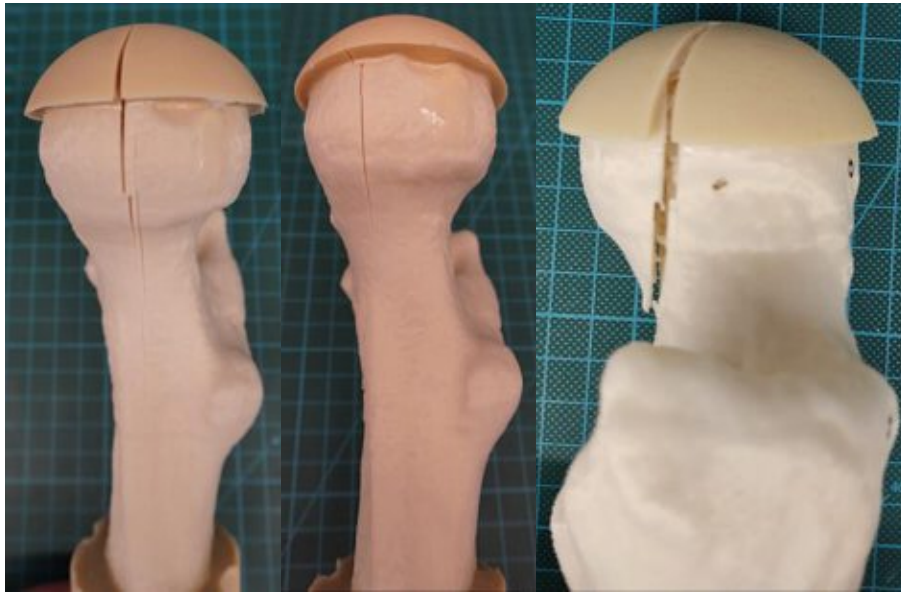


Figure 36: From left to right Type 1, Type 2, Type 3 of Femur 1

3.3 Influence of different bone sizes

This chapter investigates the behavior of different femurs. For this purpose, *Type 3* of *Femur 1-3* was tested in comparison with each other, because this represents the real bone most accurately. Figure 37 shows the load displacement curve of the selected three femora, the results of the individual test sets can be found in the Appendix A.

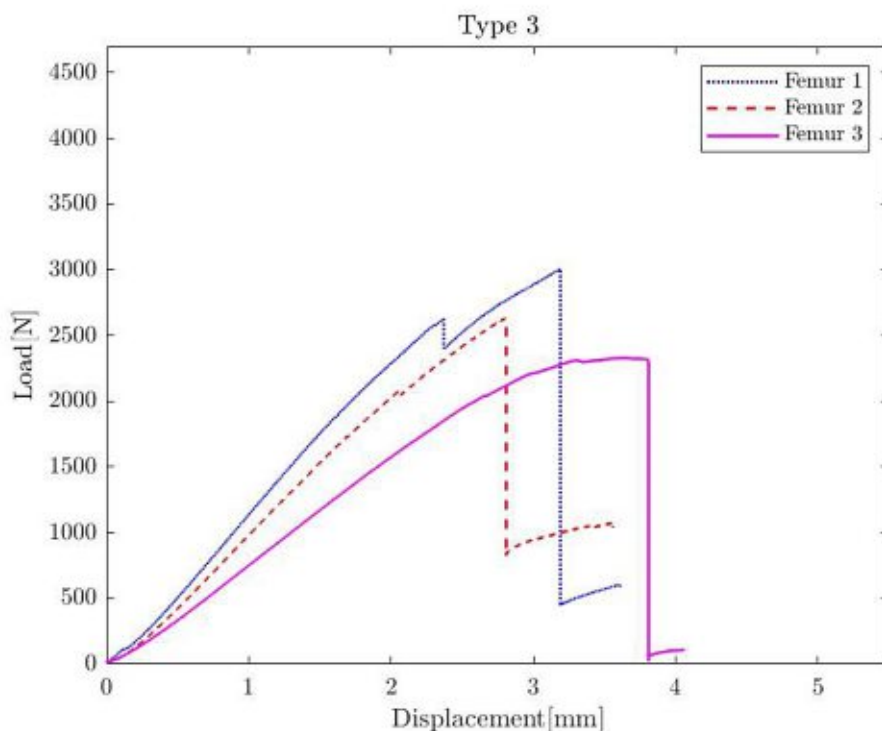


Figure 37: Results of Type 3 for all three femora.

Femur 1, with the highest density, shows a high maximum force with a previous small spike. *Type 2*, with intermediate density, has a maximum force in between the other two types. The slope of *Femur 3* has the expected course. After the linear region, there is a plastic region and with reaching the maximum force, the force level decreases abruptly.

Table 19: Maximum force and stiffness of all *Type 3* of all femora with the mean value with standard deviation.

	Min.	Max.	Mean with SD
Femur 1 max. force in N	2193.79	3006.17	2535 ± 344
Femur 1 stiffness in N/mm	1201	1364	1271 ± 68
Femur 2 max. force in N	2526.57	2629.71	2569 ± 44
Femur 2 stiffness in N/mm	1001	1205	1093 ± 84
Femur 3 max. force in N	2285.59	2439.82	2352 ± 65
Femur 3 stiffness in N/mm	834	940	885 ± 43

Table 19 shows the minimum and maximum value, as well as the mean value with standard deviation (SD) of the ultimate force and stiffness for all *Type 3* of all femora.



Figure 38: From left to right Femur 1, Femur 2, Femur 3 of all femora.

As shown in Figure 38 *Femur 1* and *2* crack at the head, but the fractures extend to the neck, therefore these fractures can be classified as simple transcervical neck fractures. The fracture of *Femur 3* is more localized at the neck and does not show splitting of the head and can be classified as displaced neck fracture. The fracture is thus larger, and the infill of the bone is clearly visible. This is also reflected in the force displacement curve.

3.4 Comparison with real bones

Since, as previously described, *Type 3* reproduces the femora most realistically, the results of these 3D printed bones are compared with those of the real bones. Figure 39 shows the load displacement curve of *Type 3* for all three 3D printed femora and those of the real femora. The results of the real bones were derived from the study by Dall'Ara [20].

The solid line represents the 3D printed bones and the dashed line the real bone. Each color represents one femur. Both the stiffness and strength of the 3D printed bones show the same trend as the real bones. The denser the femur, the higher the maximum force and stiffness. However, it should be noted that the values of the 3D printed samples are much lower compared to the real bones.

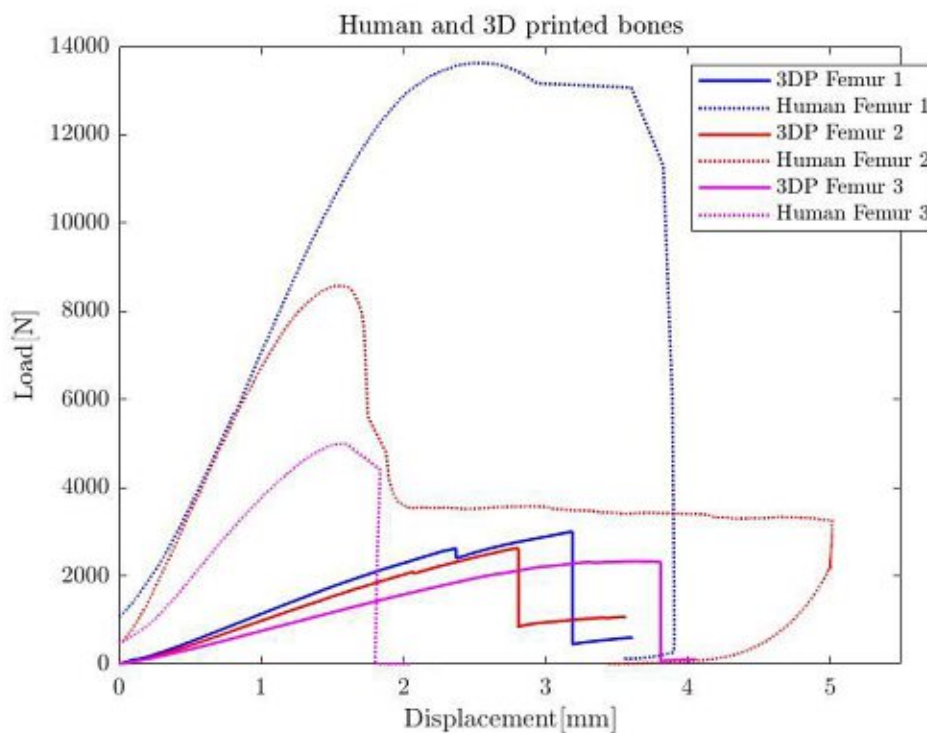


Figure 39: Results of Type 3 for all three femora and results of all three real femora.

For a better overview and to provide a direct comparison, the results of the maximum force and the stiffness are presented in bar charts.

The bar chart in Figure 40 shows the maximum force of the real femora (1- 3) in direct comparison to the mean values of the maximum force of the 3D printed bones. The difference in the maximum force of the real bones is noticeable. For the 3D printed bones, the range is smaller in which the maximum force is located.

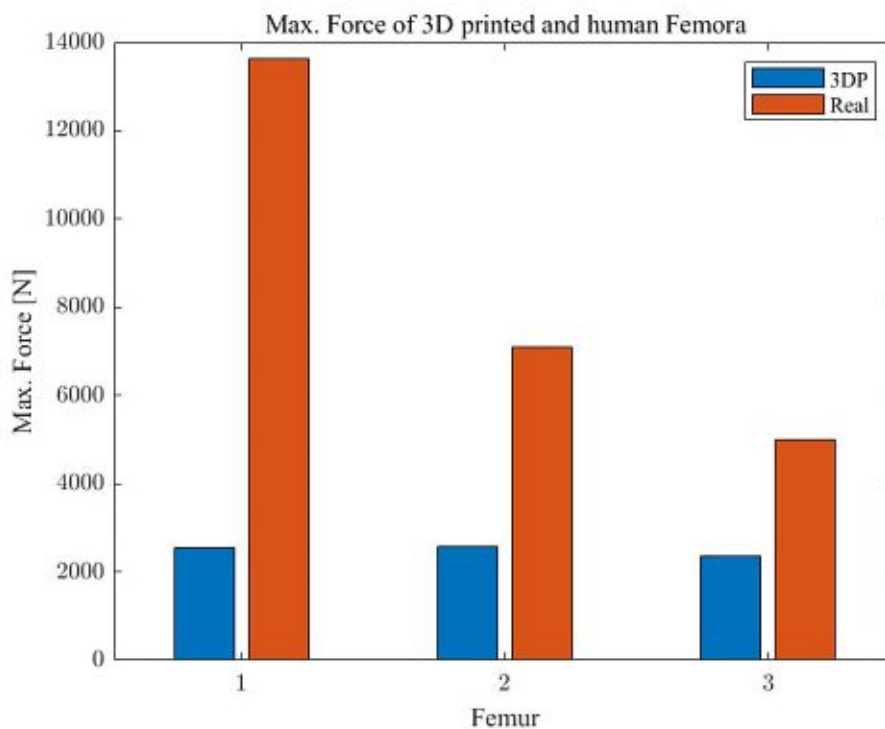


Figure 40: Mean value of the max. force of the 3D printed bones and max. force of the real bones.

The bar chart in Figure 41 shows the stiffness of the real femora (1- 3) in direct comparison to the mean values of the stiffness of the 3D printed bones. In this case, the difference is also clearly visible in the real bones as well, but the gradation between the individual femora is smaller than in the maximum force. For the 3D printed bones, the range is smaller in which the stiffness is located.

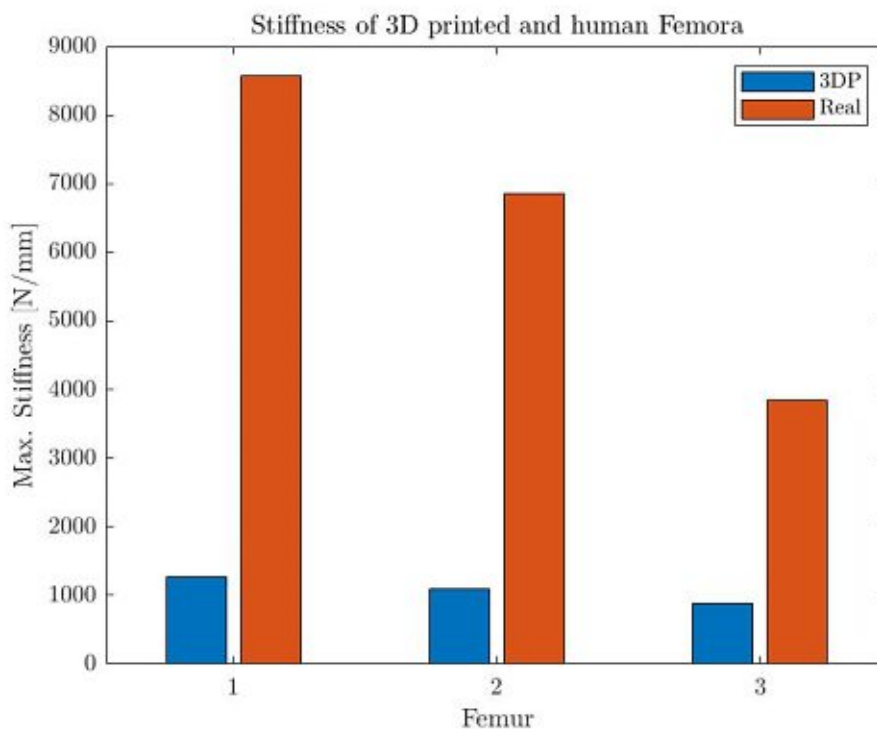


Figure 41: Mean value of the stiffness of the 3D printed bones and stiffness of the real bones.

Table 20 shows the results of the 3D printed bones, as mean values with standard deviation, and those of the real bones. Both stiffness and maximal force show the same trend as the real bones. However, as expected, the 3D printed specimens have much lower values.

Table 20: Results of the experiments of the three real femora

	Max. force in N	Stiffness in N/mm
Real Femur 1	13620	8568
3D printed Femur 1	2535±344	1271 ± 68
Real Femur 2	7092	6861
3D printed Femur 2	2569±44	1093 ± 84
Real Femur 3	4992	3837
3D printed Femur 3	2352±65	885 ± 43

4 Discussion

The aim of this study how close 3D printed bones can be replicate real bones and to evaluate how 3D printed bones behave compared to real bones. In more detail, investigate how the cortical thickness and the accurate mapping of the density areas of 3D printed bones have an influence on the biomechanical performance. Proximal femora could be successfully printed and biomechanically tested. Overall, it was found that the reproduction of realistic bones with 3D printing technology is possible in terms of cortical thickness and variable bone density in the trabecular region. In addition, this study showed that the behavior of the 3D printed bones is resembling that of the real bones. However, the values of maximum force and stiffness of the printed bones are significantly lower than those of real bones due to low stiffness of the used standard PLA 3D printing material.

The experiments were divided into various parts. In the first part, the reproduction accuracy of one type was investigated. In the second part three different types of a femur were tested. The third part includes testing of one type based on three different femora samples. Finally, the 3D printed and the real bones were compared in terms of their mechanical behavior. The experiments started with the different types of a femur in order to find out which type is best suited for the further procedure. In total, 15 3D printed bones were tested under compression, of which nine replicated *Femur 1*, three replicated *Femur 2*, and three replicated *Femur 3*.

Most of the bones had a non-realistic fracture mode, visible as splitting at the head. This occurs due to the breaking of the weak connections between the individual layers and can be caused by poor layer adhesion. This splitting can be defined as brittle and is caused by several factors. The splitting leads to a change in maximum force, but not in stiffness. It was observed in nearly all bones that the cortex (in the head/ neck region) is the weak spot, and the layers detach from one another causing a fracture. Since the bones were printed horizontally, the fibers of the cortex are aligned along the force application. As the 3D printer applies layer by layer and due to the size of the bone, the layer has already cooled down before the next one is applied, especially when printing two bones at once. As a result, the individual layers adhere less well to each other.

The *gyroid* infill reproduces the real trabecular center quite well. Real bones can interact under load and redirect the force. In nature, the fibers align themselves according to the impact of the force, this can be a reason for the fracture types. The breaking behavior of the real femora used

in this study are classified as neck fracture. This is not the case with the 3D printed bones due to splitting at the head.

The embedding of the head has a great influence on the results. A pre-test, of which the results can be found in the Appendix A, was conducted to investigate whether embedding of the head is necessary.



Figure 42: Splitting of the test bone with a non-embedded head.

Finding of the pre- test was, that without embedding the femur shows very low load absorption and in a major splitting of the head, as shown in Figure 42. Embedding the head results in better retention of the individual layers and better preservation of the contact surface.

The obtained results may also be related to the material and the printing technology and should be investigated in further studies. For this reason, FDM was compared with SLA and PLA with PET in a supplementary study. In addition, a commercially available artificial bone was used for comparison, all details of which can be found in the Appendix B.

4.1 Influence of reproduction accuracy

Three bones of each type or femur were printed and compared with each other in order to investigate the accuracy of reproducibility. The stiffnesses have a low standard deviation and a good correlation within the test sets. The values of the maximum force vary strongly within the test sets. The reason is the non-physical fracture type (layer splitting). Improved layer adhesion should overcome this issue and lead to more consistent results. Due to the more physical fracture in the neck region, a higher maximum force was reached. The pre-fractures and the fracture modes can influence the maximum force, for this reason this value should be considered with reservation.

4.2 Influence of different printing types

The constant cortex and infill is a possible reason why *Type 1* has a higher maximum force compared to the other two types. This type has a linear behavior until fracture, there is no previous splitting of the structure. This causes the bone to be very stiff compared to the other two types, and the material behaves linear until fracture. Due to the homogeneous distribution of the material the fracture occurs at the same location within the test set. The femoral head of this type has a thicker cortex than the real bone since it is calculated from the average thickness of the real cortex, as previously described. The real cortex, however, is thinner at the femoral head and thicker at the shaft. *Type 1* is with this simplification able to withstand a higher amount of load. *Type 2*, on the other hand, has a variable cortex, this means that the cortex is thinner in some areas and slightly thicker in others. Due to the constant infill, this bone is also slightly stiffer compared to *Type 3*. In *Type 3*, as in *Type 2*, pre-fractures occur, which weaken the bone and lead faster to a maximum force. The different density areas of the bone include areas without filling. This inhomogeneity results in less stiffness of the bone. To summarize, one can say that there is a visible difference between the three types. The accurate mapping of the density areas of the bone, as well as the accurate representation of the cortex thickness has an impact on the measured properties of the bones. In the results, it can be clearly seen that the simplified representation of the cortex based on the mean thickness leads to a higher stiffness and maximum force. The mean values of *Type 2* and *3* for both maximum force and stiffness are in one range. This indicates that a correct cortical thickness is more important and that a precise representation of a varying infill has a minor impact on the overall biomechanical outcomes.

4.3 Influence of different bone sizes

For the reasons mentioned above, *Type 3* of different femora was compared for the further process of the work.

The real *Femur 1* is the most dense, which is also reflected in the 3D printed bone. The mapped areas of cancellous bone are larger and with a higher infill percentage than *Femur 2* and *3*, which explains the higher stiffness of *Femur 1*.

It is noticeable that *Femur 3* shows an almost plastic area in one of the tests. The femur does not split at the head during fracture but breaks in the direction of the neck. This represents a realistic fracture mode, since no splitting occurs, and the layer adhesion has a minor effect.

There is a difference between the individual femora, and it is related to the real density of the bone in terms of maximum force and stiffness. Less dense filling results in lower mechanical properties. However, the values of the two measured properties for the 3D printed bones are still close to each other.

4.4 Comparison with real bones

Type 3 was used to compare the 3D printed bones with the real bones. The maximum force and stiffness of all three real bones is significantly higher than those of the 3D printed ones. As expected, the data of the real and the 3D printed bones are not in the same range.

Real bones have a cartilage layer which has a great influence on the mechanical behavior [20]. The reason of this is that a bone is normally fatty and excretes secretion, which influences the mechanical properties. These facts usually decrease the measured stiffness. However, the bone tissue of real bones is much stiffer and stronger than the used printing PLA material. The real bones show a strong correlation of density with maximum force and stiffness. The denser the bone, the higher the maximum force and stiffness. The same but less pronounced observation was made for the 3D printed bones.

With higher densities, the results of the real and the 3D-printed bones are further apart. The maximum force of the real *Femur 1* is over five times higher compared to the 3D printed bone, whereas the maximum force of the real *Femur 3* is only slightly over twice as high compared to the 3D printed bone. Thus, it can be noted that the behavior of the 3D printed bones is resembling in a certain sense that of the real bones. The denser the bone, the higher the maximum force and stiffness.

4.5 Conclusions and Outlook

In conclusion, it is possible to reproduce realistic bones with the 3D printing technique, in terms of cortical thickness and variable bone density in the trabecular region. The accurate mapping of the density areas showed a minor influence on the structural outcome whereas a correct modelling of the cortex is important. Compared to the real bones, the results of the 3D printed bones are significantly lower because of the considerably lower bulk material properties of PLA compared to the tissue of real bones. It was also shown that the FDM process is well suited for reprinting bones, as it is fast and cost-effective. Using FDM printing also has the advantage that the density areas can be defined quite precisely in the slicing software, which is more difficult

to achieve with other printing methods. Nevertheless, further studies should investigate if better results can be achieved with other printing technologies and other materials.

However, for future studies, further adaptation of the parameters for 3D printing is recommended to achieve better mechanical behavior. Conceivable here would be the use of a larger extrusion width of 0.6mm instead of 0.42mm, an increased printing temperature of around 225°C and a closer approach of the nozzle to 0.2mm instead of 0.3mm, using the same material. These changed settings could result in less splitting of the material during testing. Another possibility is a different configuration of the cooling, which could lead to a more brittle material.

The production of the bones with the FDM method and PLA is sufficient for an initial overview of the different bone types. However, for further studies, other printing parameters and materials could be studied to obtain a more suitable result.

References

- [1] P. G. McMenamin, M. R. Quayle, C. R. McHenry, and J. W. Adams, “The production of anatomical teaching resources using three-dimensional (3D) printing technology,” *Anatomical sciences education*, vol. 7, no. 6, pp. 479–486, 2014, doi: 10.1002/ase.1475.
- [2] A. Gebhardt, J.-S. Hötter, and M. Fateri, Eds., *Generative Fertigungsverfahren: Additive manufacturing und 3D Drucken für Prototyping - Tooling - Produktion*, 4th ed. München: Hanser, 2013.
- [3] S. C. Cowin, *Bone mechanics handbook*, 2nd ed. Boca Raton: CRC Press, 2001.
- [4] E. N. Marieb and K. Hoehn, Eds., *Human anatomy & physiology*, 9th ed. Boston: Pearson, 2013.
- [5] M. Schünke, E. Schulte, U. Schumacher, M. Voll, and K. H. Wesker, Eds., *PROMETHEUS Allgemeine Anatomie und Bewegungssystem*. Stuttgart: Georg Thieme Verlag, 2018.
- [6] M. Hutchinson and R. T. Hutchings, Eds., *A brief atlas of the human body: Für Naturwissenschaftler, Chemiker und Ingenieure*, 2nd ed. San Francisco, Calif.: Pearson Benjamin Cummings, 2007.
- [7] X. Wang, J. S. Nyman, X. Dong, H. Leng, and M. Reyes, Eds., *Fundamental Biomechanics in Bone Tissue Engineering*, 2010.
- [8] D. H. Pahr and A. G. Reisinger, “A Review on Recent Advances in the Constitutive Modeling of Bone Tissue,” *Current osteoporosis reports*, pp. 696–704.
- [9] P. Fratzl and R. Weinkamer, “Nature’s hierarchical materials,” *Progress in Materials Science*, pp. 1263–1334.
- [10] A. V. Rammohan and V. B. C. Tan, “Morphological models of trabecular bone suitable for high-porosity regions and vertebrae,” *Computer methods in biomechanics and biomedical engineering*, vol. 19, no. 13, pp. 1418–1422, 2016, doi: 10.1080/10255842.2016.1146945.
- [11] R. Oftadeh, M. Perez-Viloria, J. C. Villa-Camacho, A. Vaziri, and A. Nazarian, “Biomechanics and mechanobiology of trabecular bone: a review,” *Journal of biomechanical engineering*, vol. 137, no. 1, 2015, doi: 10.1115/1.4029176.

- [12] Nelly Shafik Ramzy, “Sustainable spaces with psychological connotation: Historical architecture as reference book for biomimetic models with biophilic qualities,” *Archnet-IJAR*, Volume 9 - Issue 2, pp. 248–267, Jul. 2015.
- [13] Rho J., Kuhn-Spearing L., Zioupos P., “Mechanical properties and the hierarchical structure of bone,” *Medical Engineering & Physics*, pp. 92–102.
- [14] J. K. Gong, J. S. Arnold, and S. H. Cohn, “Composition of trabecular and cortical bone,” *The Anatomical Record*, no. 149.3, pp. 325–331, 1964.
- [15] T. Kokubo, H.-M. Kim, and M. Kawashita, “Novel bioactive materials with different mechanical properties,” *Biomaterials*, vol. 24, no. 13, pp. 2161–2175, 2003, doi: 10.1016/S0142-9612(03)00044-9.
- [16] D. T. Reilly and A. H. Burstein, “The elastic and ultimate properties of compact bone tissue,” *Journal of biomechanics*, vol. 8, no. 6, pp. 393–405, 1975, doi: 10.1016/0021-9290(75)90075-5.
- [17] C. Ross Ethier and Craig A. Simmons, Ed., *Introductory Biomechanics: From Cells to Organisms*.
- [18] M. Papini, R. Zdero, E. H. Schemitsch, and P. Zalzal, “The biomechanics of human femurs in axial and torsional loading: comparison of finite element analysis, human cadaveric femurs, and synthetic femurs,” *Journal of biomechanical engineering*, vol. 129, no. 1, pp. 12–19, 2007, doi: 10.1115/1.2401178.
- [19] G. Iori *et al.*, “Femur strength predictions by nonlinear homogenized voxel finite element models reflect the microarchitecture of the femoral neck,” *Medical Engineering & Physics*, vol. 79, pp. 60–66, 2020, doi: 10.1016/j.medengphy.2020.03.005.
- [20] E. Dall'Ara, B. Luisier, R. Schmidt, F. Kainberger, P. Zysset, and D. Pahr, “A nonlinear QCT-based finite element model validation study for the human femur tested in two configurations in vitro,” *Bone*, pp. 27–38.
- [21] E. Dall'Ara *et al.*, “DXA predictions of human femoral mechanical properties depend on the load configuration,” *Medical Engineering & Physics*, vol. 35, no. 11, 1564–72; discussion 1564, 2013, doi: 10.1016/j.medengphy.2013.04.008.
- [22] S. Waldt, M. Eiber, and K. Wörtler, Eds., *Messverfahren und Klassifikationen in der muskuloskelettalen Radiologie: 75 Tabellen*, 2nd ed. Stuttgart: Thieme, 2017.
- [23] L. Cristofolini, M. Juszczuk, S. Martelli, F. Taddei, and M. Viceconti, “In vitro replication of spontaneous fractures of the proximal human femur,” *Journal of biomechanics*, vol. 40, no. 13, pp. 2837–2845, 2007, doi: 10.1016/j.jbiomech.2007.03.015.

- [24] O. Johnell and J. A. Kanis, “An estimate of the worldwide prevalence and disability associated with osteoporotic fractures,” *Osteoporosis international : a journal established as result of cooperation between the European Foundation for Osteoporosis and the National Osteoporosis Foundation of the USA*, vol. 17, no. 12, pp. 1726–1733, 2006, doi: 10.1007/s00198-006-0172-4.
- [25] Y. Luo, “Bone Density and Mechanical Property,” pp. 31–44, doi: 10.1007/978-3-319-51671-4_4.
- [26] E. G. Meinberg, J. Agel, C. S. Roberts, M. D. Karam, and J. F. Kellam, “Fracture and Dislocation Classification Compendium-2018,” *Journal of orthopaedic trauma*, 32 Suppl 1, S1-S170, 2018, doi: 10.1097/BOT.0000000000001063.
- [27] AO Foundation Switzerland, *AO/OTA Fracture and Dislocation Classification: Long-bone fractures*.
- [28] J. E. Adams, “Quantitative computed tomography,” *European journal of radiology*, vol. 71, no. 3, pp. 415–424, 2009, doi: 10.1016/j.ejrad.2009.04.074.
- [29] K. Engelke *et al.*, “Clinical Use of Quantitative Computed Tomography-Based Advanced Techniques in the Management of Osteoporosis in Adults: the 2015 ISCD Official Positions-Part III,” *Journal of clinical densitometry : the official journal of the International Society for Clinical Densitometry*, vol. 18, no. 3, pp. 393–407, 2015, doi: 10.1016/j.jocd.2015.06.010.
- [30] M. Amini, A. Reisinger, and D. H. Pahr, “Influence of processing parameters on mechanical properties of a 3D-printed trabecular bone microstructure,” *Journal of biomedical materials research. Part B, Applied biomaterials*, vol. 108, no. 1, pp. 38–47, 2020, doi: 10.1002/jbm.b.34363.
- [31] D. H. Pahr and P. K. Zysset, “From high-resolution CT data to finite element models: development of an integrated modular framework,” *Computer methods in biomechanics and biomedical engineering*, vol. 12, no. 1, pp. 45–57, 2009, doi: 10.1080/10255840802144105.
- [32] T. D. Ngo, A. Kashani, G. Imbalzano, K. T. Nguyen, and D. Hui, “Additive manufacturing (3D printing): A review of materials, methods, applications and challenges,” *Composites Part B: Engineering*, vol. 143, pp. 172–196, 2018, doi: 10.1016/j.compositesb.2018.02.012.
- [33] C.-Y. Liaw and M. Guvendiren, “Current and emerging applications of 3D printing in medicine,” *Biofabrication*, vol. 9, no. 2, p. 24102, 2017, doi: 10.1088/1758-5090/aa7279.

- [34] Allie Nawrat, “3D printing in the medical field: four major applications revolutionising the industry,” *Verdict Medical Devices*, 07 Aug., 2018.
- [35] Y. Huang, M. C. Leu, J. Mazumder, and A. Donmez, “Additive Manufacturing: Current State, Future Potential, Gaps and Needs, and Recommendations,” *Journal of Manufacturing Science and Engineering*, vol. 137, no. 1, 2015, doi: 10.1115/1.4028725.
- [36] *ASTM F2792-12, Standard Terminology for Additive Manufacturing Technologies*, F42 Committee, West Conshohocken, PA.
- [37] N. Shahrubudin, T. C. Lee, and R. Ramlan, “An Overview on 3D Printing Technology: Technological, Materials, and Applications,” *Procedia Manufacturing*, vol. 35, pp. 1286–1296, 2019, doi: 10.1016/j.promfg.2019.06.089.
- [38] F. P. W. Melchels, J. Feijen, and D. W. Grijpma, “A review on stereolithography and its applications in biomedical engineering,” *Biomaterials*, vol. 31, no. 24, pp. 6121–6130, 2010, doi: 10.1016/j.biomaterials.2010.04.050.
- [39] F. Calignano *et al.*, “Overview on Additive Manufacturing Technologies,” *Proc. IEEE*, vol. 105, no. 4, pp. 593–612, 2017, doi: 10.1109/JPROC.2016.2625098.
- [40] K.-Y. Lee *et al.*, “Accuracy of three-dimensional printing for manufacturing replica teeth,” *Korean journal of orthodontics*, vol. 45, no. 5, pp. 217–225, 2015, doi: 10.4041/kjod.2015.45.5.217.
- [41] Prusa Research s.r.o., *PETG_DataSheet*.
- [42] Prusa Research s.r.o., *ASA_DataSheet*.
- [43] K. Modjarrad and S. Ebnesajjad, *Handbook of Polymer Applications in Medicine and Medical Devices: Plastics Used in Medical Devices*. Amsterdam: Elsevier/WA, 2013.
- [44] Prusa Research s.r.o., *PLA_Datasheet*.
- [45] G. Hsiang Loh, E. Pei, J. Gonzalez-Gutierrez, and M. Monzón, “An Overview of Material Extrusion Troubleshooting,” *Applied Sciences*, vol. 10, no. 14, p. 4776, 2020, doi: 10.3390/app10144776.
- [46] E. Alabort, D. Barba, and R. C. Reed, “Design of metallic bone by additive manufacturing,” *Scripta Materialia*, vol. 164, pp. 110–114, 2019, doi: 10.1016/j.scriptamat.2019.01.022.
- [47] L. Germain, C. A. Fuentes, A. W. van Vuure, A. Des Rieux, and C. Dupont-Gillain, “3D-printed biodegradable gyroid scaffolds for tissue engineering applications,” *Materials & Design*, vol. 151, pp. 113–122, 2018, doi: 10.1016/j.matdes.2018.04.037.

- [48] S. Ma, Q. Tang, Q. Feng, J. Song, X. Han, and F. Guo, “Mechanical behaviours and mass transport properties of bone-mimicking scaffolds consisted of gyroid structures manufactured using selective laser melting,” *Journal of the mechanical behavior of biomedical materials*, vol. 93, pp. 158–169, 2019, doi: 10.1016/j.jmbbm.2019.01.023.
- [49] A. Yáñez, A. Cuadrado, O. Martel, H. Afonso, and D. Monopoli, “Gyroid porous titanium structures: A versatile solution to be used as scaffolds in bone defect reconstruction,” *Materials & Design*, vol. 140, pp. 21–29, 2018, doi: 10.1016/j.matdes.2017.11.050.
- [50] A. Yáñez, A. Herrera, O. Martel, D. Monopoli, and H. Afonso, “Compressive behaviour of gyroid lattice structures for human cancellous bone implant applications,” *Materials science & engineering. C, Materials for biological applications*, vol. 68, pp. 445–448, 2016, doi: 10.1016/j.msec.2016.06.016.
- [51] A. Gebhardt, J. Kessler, and L. Thurn, *3D Printing: Understanding Additive Manufacturing*, 2nd ed. Cincinnati, Ohio: Hanser Publications, 2018.
- [52] M. Bartikian, A. Ferreira, A. Gonçalves-Ferreira, and L. L. Neto, “3D printing anatomical models of head bones,” *Surgical and radiologic anatomy : SRA*, vol. 41, no. 10, pp. 1205–1209, 2019, doi: 10.1007/s00276-018-2148-4.
- [53] R. E. Rebong, K. T. Stewart, A. Utreja, and A. A. Ghoneima, “Accuracy of three-dimensional dental resin models created by fused deposition modeling, stereolithography, and Polyjet prototype technologies: A comparative study,” *The Angle orthodontist*, vol. 88, no. 3, pp. 363–369, 2018, doi: 10.2319/071117-460.1.
- [54] N. Xu *et al.*, “3D artificial bones for bone repair prepared by computed tomography-guided fused deposition modeling for bone repair,” *ACS applied materials & interfaces*, vol. 6, no. 17, pp. 14952–14963, 2014, doi: 10.1021/am502716t.
- [55] J. Kang *et al.*, “Custom design and biomechanical analysis of 3D-printed PEEK rib prostheses,” *Biomechanics and modeling in mechanobiology*, vol. 17, no. 4, pp. 1083–1092, 2018, doi: 10.1007/s10237-018-1015-x.
- [56] Dr. Pahr Ingenieure e.U, *Medtool Manual 4.5*. [Online]. Available: <http://www.dr-pahr.at/html/index.html>
- [57] D. H. Pahr and P. K. Zysset, “A comparison of enhanced continuum FE with micro FE models of human vertebral bodies,” *Journal of biomechanics*, vol. 42, no. 4, pp. 455–462, 2009, doi: 10.1016/j.jbiomech.2008.11.028.
- [58] Prusa Research s.r.o., *Prusa3d_manual_mk3s_*.

-
- [59] Zwick GmbH & Co. KG, “Tisch-Prüfmaschinen Z030 bis Z100 der AllroundLine / Table-top machines Z030 up to Z100 of the AllroundLine,” [Online]. Available: https://www.zwickroell.com/-/media/files/sharepoint/vertriebsdoku_pi/02_201_material_pruefmaschine_allroundline_z030_bis_z100_pi_de.pdf
- [60] S. R. Goodyear and R. M. Aspden, “Mechanical properties of bone ex vivo,” *Methods in molecular biology (Clifton, N.J.)*, vol. 816, pp. 555–571, 2012, doi: 10.1007/978-1-61779-415-5_35.
- [61] kprinter, *Technische Spezifikation 3dkTopFilament*.

Appendix A

A.1 Test bones

In preliminary tests, it was investigated whether the bones should be printed horizontally or vertically. Observing the results on the left side in Figure 43, the maximum force is lower for the vertically printed bone. However, the most noticeable aspect is the fracture point, which can be seen in the middle of Figure 43. The vertically printed bone breaks flat at the shaft. However, it should be noted that the embedment at the head is not straight and this may be a cause for the low maximum force. For the further process of the study, the horizontal printing of the bones was used due to the fracture location.

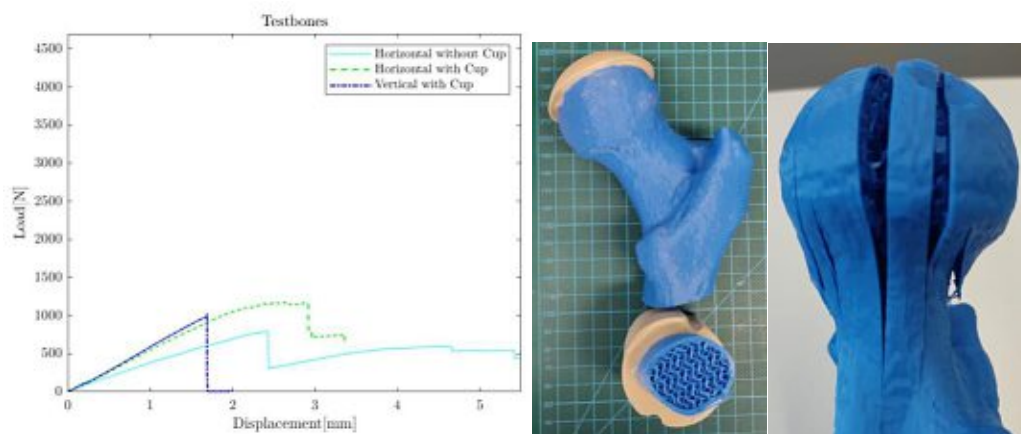


Figure 43: Left: Results of the test bones. Middle: Fracture of the vertical printed test bone. Right: Splitting of the head of the first horizontal printed testbone.

In a second series of tests, the embedding was investigated. Based on the results, shown in Figure 43, it was decided for the further process of the study that the bones are embedded at the shaft as well as at the head. The maximum force and stiffness are low compared to the bone having an additional embedment at the head. The splitting of the head, as shown on the right in Figure 43, should also be reduced by embedding the head.

For a better overview, Table 21 shows the results of maximum force and stiffness of the three test bones.

Table 21: Results of maximum force and stiffness of the test bones.

	Max. force in N	Stiffness in N/mm
Horizontal w/o cup	791.84	337
Horizontal w cup	1171.82	564
Vertical w cup	1028.79	625

A.2 Results of the test set of Femur 1 Type 1

Each of the three types of *Femur 1* was printed and tested three times. The procedure of printing, post-processing and testing is described in the previous chapters.

Figure 44 shows the results of *Type 1* in comparison with each other. The course of the three tests is identical, so the difference in stiffness is infinitesimally small. The difference in the maximum force is more noticeable. A remarkable fact about this type is that the fracture looks the same in all three tests. The fracture extends once through the head, as can be seen on the right side of Figure 44.

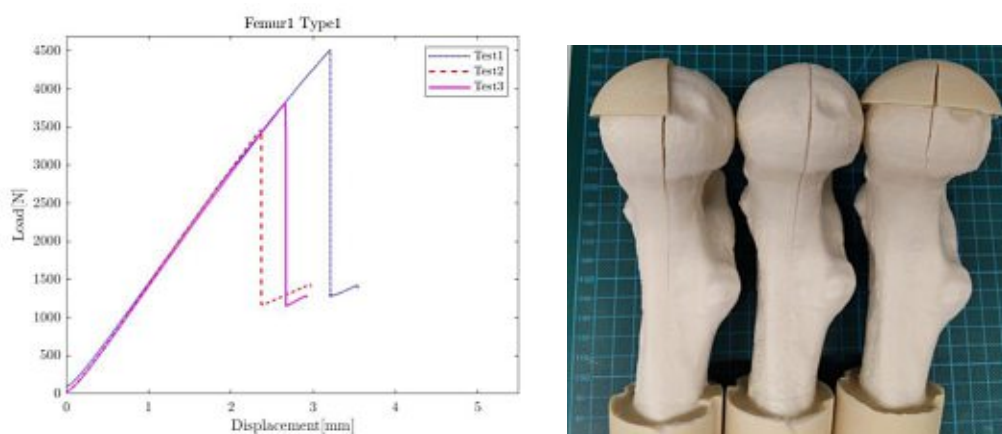


Figure 44: Left: Results of Type 1 of Femur 1. Right: Type 1 of Femur 1 of all test runs, from left to right: test 1, test 2, test 3

Table 22 shows the maximum force, as well as the stiffness for all three tests of *Femur 1 Type 1*. Test 1 had the highest maximum force, but the lowest stiffness.

Table 22: Maximum force and stiffness of the test set of Type 1 of Femur 1.

	Max. force in N	Stiffness in N/mm
Test 1	4515.30	1363
Test 2	3471.31	1498
Test 3	3820.87	1502

A.3 Results of the test set of Femur 1 Type 2

Figure 45 shows the results of *Type 2* in comparison with each other. The course of the three tests is almost identical, so the differences in stiffness and maximum force are small. The right side of Figure 45 shows the fracture locations of *Type 2* of the three test runs. The fracture points of test 2 and test 3 are very similar and show a splitting of the head, like in *Type 1*. In contrast, the fracture point of test 1 is located more in the direction of the neck. In the force-displacement curve, a plastic deformation can also be seen for test 1 after splitting.

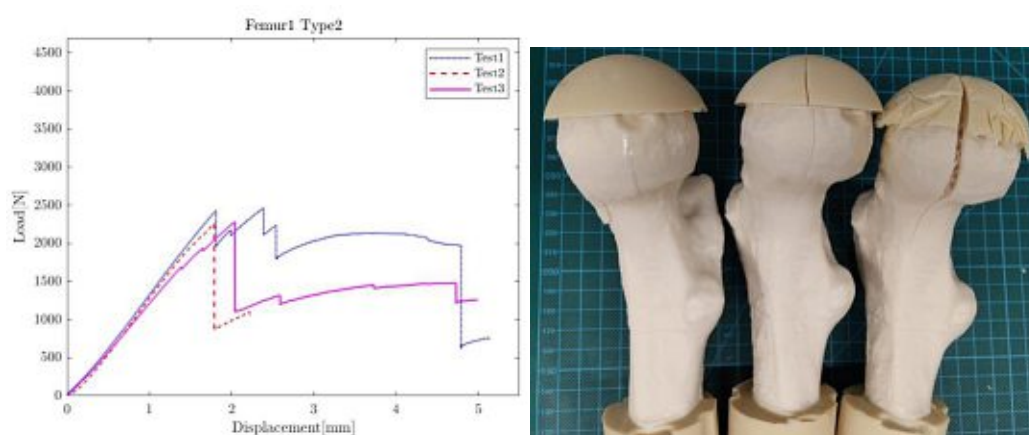


Figure 45: Left: Results of *Type 2* of *Femur 1*. Right: *Type 2* of *Femur 1* of all test runs, from left to right: test 1, test 2, test 3

Table 23 shows the maximum force, as well as the stiffness for all three tests of *Femur 1 Type 2*. The stiffness of test 1 and 3 is identical.

Table 23: Maximum force and stiffness of the test set of *Type 2* of *Femur 1*.

	Max. force in N	Stiffness in N/mm
Test 1	2459.72	1247
Test 2	2262.52	1362
Test 3	2285.02	1246

A.4 Comparison of the results of Femur 1

When comparing the averages of the three different types, it can be seen, as shown in Figure 46, that *Type 1* has the maximum force absorption and the highest stiffness. Additionally, Table 24 shows the coefficient of variation for the maximum force and stiffness of the three types of *Femur 1* based on the mean values and standard deviation from the test sets. The value shows the dispersion of the mean value. The coefficient of variation of *Type 1* and 3 is above 10 %, which indicates a large spread of the values.

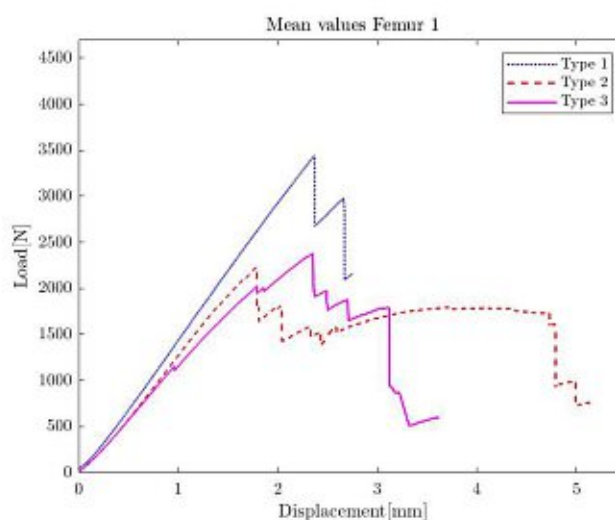


Figure 46: Mean values of all types of *Femur 1*

For a better overview, Table 24 shows the mean values with standard deviation of each type of *Femur 1*.

Table 24: Average and coefficient of variation of maximum force and stiffness for all three types of *Femur 1*.

	Average max. force in N	Average stiffness in N/mm	Variation of force in %	Variation of stiffness in %
Femur 1 Type 1	3936±434	1449±29	11	4
Femur 1 Type 2	2336±344	1326±88	4	7
Femur 1 Type 3	2535±344	1255±31	14	5

A.5 Results of the test set of Femur 2 Type 3

Figure 47 shows the results of *Type 3* in comparison with each other. The course of the three tests is slightly different, therefore there is also a difference in stiffness. However, the maximum force is very similar for all three test runs. The right side of Figure 47 shows the fracture locations of *Type 3* of the three test runs. The fracture points of all test runs are very similar and show a splitting in the side.

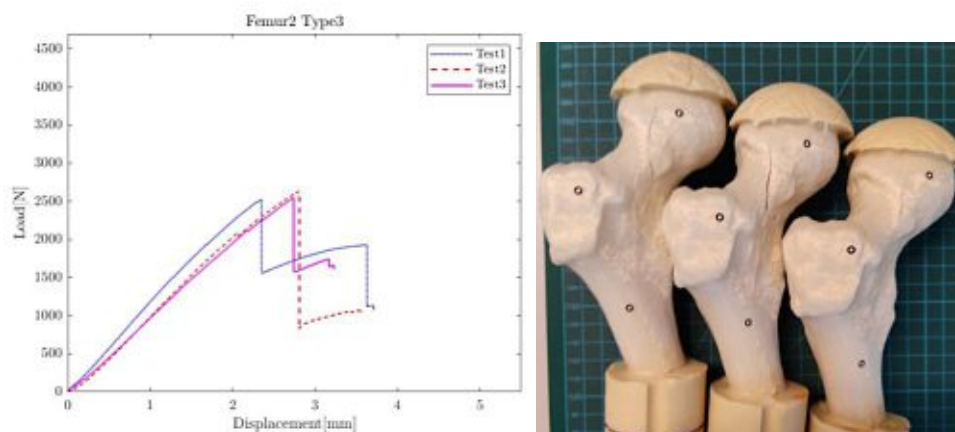


Figure 47: Left: Results of *Femur 2 Type 3*. Right: *Type 3* of *Femur 2* of all test runs, from left to right: test 1, test 2, test 3

Table 25 shows the maximum force, as well as the stiffness for all three tests of *Femur 2 Type 3*. The maximum force of all three test sets is almost the same.

Table 25: Maximum force and stiffness of the test set of *Type 3* of *Femur 2*.

	Max. force in N	Stiffness in N/mm
Test 1	2526.57	1205
Test 2	2629.71	1072
Test 3	2549.03	1001

A.6 Results of the test set of Femur 3 Type 3

Figure 48 shows the results of *Type 3* in comparison with each other. The course of the test 1 and 2 is almost identical, therefore there is only a slightly difference in stiffness. The slope of test 3 has the expected course. However, the maximum force is very similar for all three test runs. The right side of Figure 48 shows the fracture locations of *Type 3* of the three test runs. The fracture points of test 1 and 2 are very similar and show a splitting in the side. The fracture of test 3 is more localized at the neck.

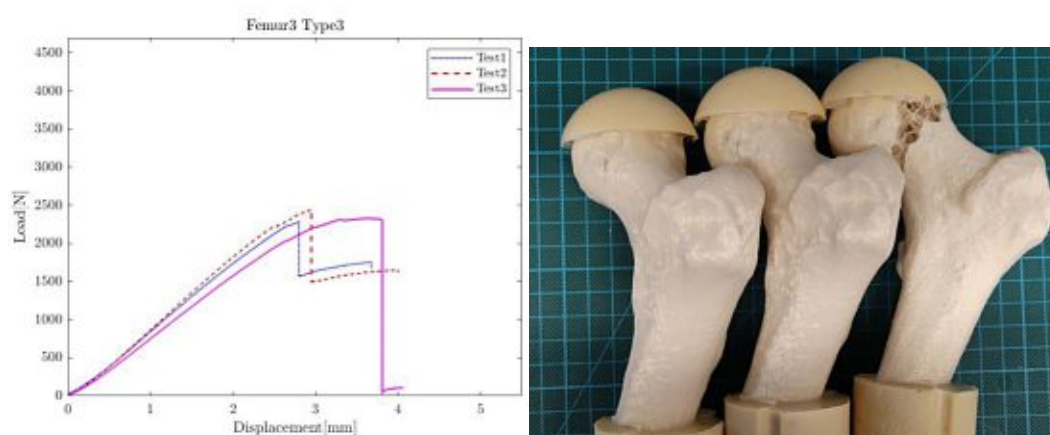


Figure 48: Left: Results of *Femur 3 Type 3*. Right: *Type 3* of *Femur 3* of all test runs, from left to right: test 1, test 2, test 3

Table 26 shows the maximum force, as well as the stiffness for all three tests of *Femur 3 Type 3*. The stiffness of the test set is low compared to the other two femora.

Table 26: Maximum force and stiffness of the test set of *Type 3* of *Femur 3*.

	Max. force in N	Stiffness in N/mm
Test 1	2285.59	882
Test 2	2439.82	940
Test 3	2330.97	834

A.7 Comparison of the results of Type 3

For a better overview, Table 27 shows the mean values with standard deviation of each Femur of *Type 3*. When comparing the averages of the three different femora, it can be seen, as shown in Figure 49 that *Femur 1* and *2* have almost the same maximum force. The right side of Figure 49 shows *Type 3* of the three femora beside each other. The size difference of the three bones is clearly visible. *Femur 1* and *2* show splitting and *Femur 3* breaks open at the neck during one test, as described previously.

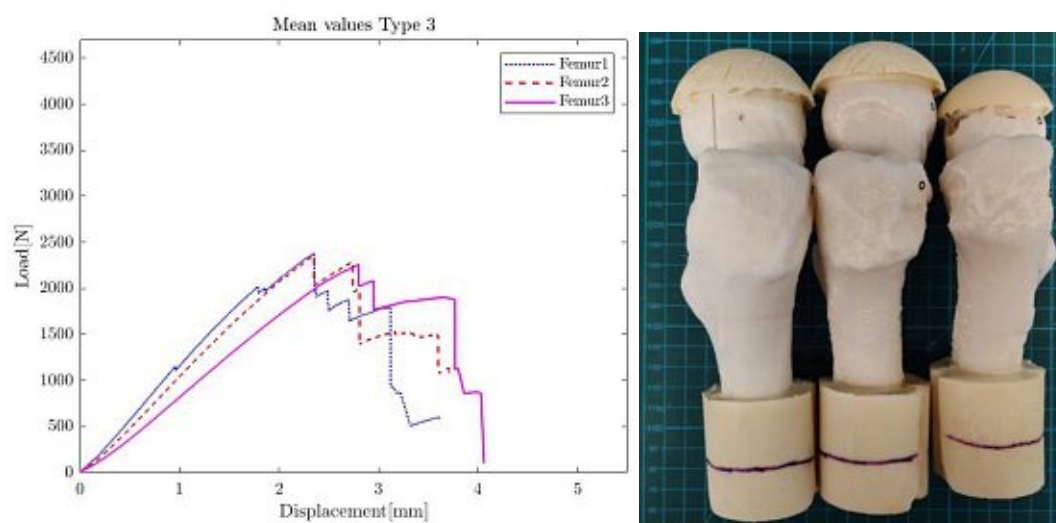


Figure 49: Left: Mean values of *Type 3* of all three femora. Right: *Type 3* of all femora. From left to right: *Femur 1*, *Femur 2*, *Femur 3*

Additionally, Table 27 shows the coefficient of variation for the maximum force and stiffness for *Type 3* of all femora based on the mean values and standard deviation from the test sets. The value shows the dispersion of the mean value. The coefficient of variation of the force for *Femur 1* is above 10 %, which indicates a large spread of the values, as described previously.

Table 27: Average and coefficient of variation of the maximum force and stiffness for *Type 3* of all femora

	Max. Force in N	Stiffness in N/mm	Variation of force in %	Variation of stiffness in %
Femur1 Type3	2535±344	1255±31	14	5
Femur2 Type3	2569±44	1100±80	2	8
Femur3 Type3	2352±65	891±52	3	5

Appendix B

B.1 Supplementary study

For a preliminary insight for further studies, three different bones were used for comparison of printing technology and material. First, *Femur 2* was printed with PET with a crystallization accelerator (Bernhardt Kunststoffverarbeitungs GmbH, Berlin, Germany). The settings were the same as for PLA, only the material and related data were changed according to the manufacturer, shown in Table 28. For post-processing, the bone was placed in the oven and completely heated through, this results in partial crystalline structures, which ensure that the material becomes stronger.

Table 28: Properties of PET according to the manufacturer [61].

Name	Chemical name	Diameter in mm	Density in g/cm ³	T _{Nozzle} in °C	T _{Heat Bed} in °C
PET	Polyethylenterephthalat	1,75	1,40	240 - 250	90 – 100

The CT data from *Femur 1* was also used as the basis for a bone printed with the SLA printer. The infill for this bone is also intended to resemble the trabecular structure. The infill is constant for this bone and the cortex is variable, therefore it is comparable to *Type 2*.

In addition, an ORTHObone (3B Scientific GmbH), a conventional artificial bone, was prepared for mechanical testing. Since the received QCT data all have a 20° angle, it is necessary for a good comparison to make sure that the ORTHObone also has this angle. The artificial bone was sawed off with 20° divergence from the mechanical axis, as described previously in chapter 2.

These three bones were also embedded at the top and bottom as previously described, with 27 mm of the shaft and with the suitable cup for the head with 20mm. The measured data of these three bones can be seen in Table 29.

Table 29: Details of the bone printed with PET and SLA printed bone and the *ORTHO*bone.

	PET	SLA	ORTHObone
Diameter shaft in mm	31	34	30
Diameter head in mm	51	54	45
Height without embedding in mm	171	-	160
Height with embedding in mm	197	177	183
Weight without embedding in g	127	167	57

Figure 50 shows that *Femur 2 Type 3*, which was printed with two different materials (PLA and PET), has a very similar course. In direct comparison with the PLA printed bone, the two materials are in a similar range in terms of maximum strength and stiffness. But the cost and post-processing time of PET are higher than PLA.

The bone printed with the SLA process has a significantly different course than the same bone produced with the FDM printer. The maximum force of the 3D printed bone and the SLA technique bone are in a very similar range. However, the stiffness of the bone printed with SLA is significantly lower, which can be explained by not enough curing time. This causes the bone to be softer and only able to withstand a lower amount of load. In addition, the structure of the infill must be programmed manually to obtain a similar structure of the trabecular bone. The manufacturing and post-processing time requires more time than that of printing with the FDM technique.

The artificial *Orthobone* has a very flat course and therefore a lower maximal force and stiffness than the other tested bones. Observing the curve of the common artificial bone, it does not behave nearly like the 3D printed bones. The elastic region until the maximum force is very wide compared to the other bones. This results in a lower stiffness. It can therefore be concluded that the printed bones for this study imitate the load-displacement curve of a real femur better than the *ORTHO*bone tested here.

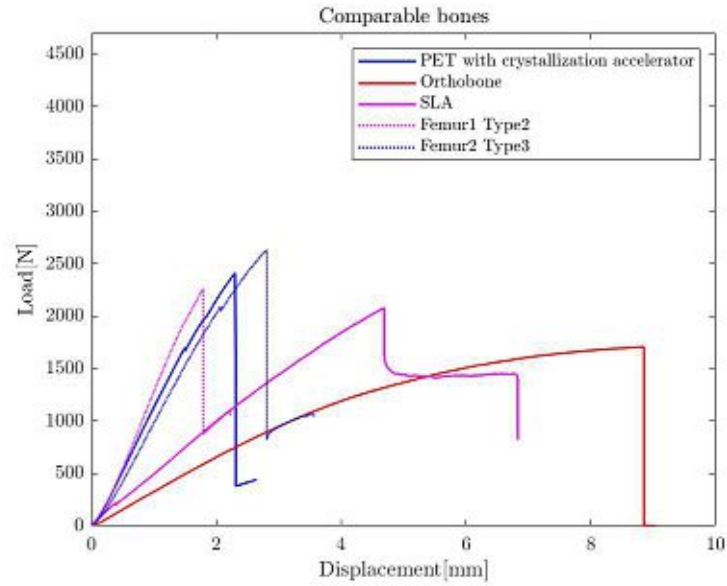


Figure 50: Top: Results of the comparable bones. Bottom: From left to right: SLA printed bone, *ORTHO*bone and *PET* printed bone

The bottom of Figure 50 shows the fracture points of the three comparable bones. The SLA printed bone cracked at the head, the *ORTHO*bone broke at the shaft and the bone printed with PET behaved similarly to the bones previously printed with PLA. All results of the comparable bones are shown in Table 30 for a better overview and direct comparison with the 3D printed bones with PLA.

Table 30: Max. force and stiffness of the comparable bones and the average of *Femur 1 Type 2* and *Femur 2 Type 3*.

	Max. Force in N	Stiffness in N/mm
Femur1 Type2 (mean value)	2235,63	1326
Femur2 Type3 (mean value)	2354,9	1100
PET	2412,48	1204
SLA	2079,63	489
<i>ORTHO</i> bone	1708,41	336